

Experimental observations and statistical modelling of crack propagation dynamics in limestone by acoustic emission analysis during freezing and thawing

Julian Murton¹ and Vikram Maji²

¹University of Sussex

²IIT Kanpur

November 24, 2022

Abstract

The timing and location of microcracking events, their propagation and coalescence to form macrocracks, and their development by tension, shearing or mixed modes are little known but essential to understanding the fracture of intact rock by freezing and thawing. The aims of the present study are to investigate the mechanisms and transition of micro- and macrocracking during repeated freeze–thaw, and to develop a statistical model of crack propagation that assesses the distance and angular relationship of neighbouring cracking events arranged in their temporal order of occurrence. Eight acoustic emission (AE) sensors mounted on a 300 mm cubic block of chalk captured the three-dimensional locations of microcracking events in their temporal order of occurrence during 16 seasonal freeze–thaw cycles simulating an active layer above permafrost. AE events occurred mostly during thawing periods (45%) and freeze-to-thaw transitions (37%) rather than during freezing periods (9%) and thaw-to-freeze transitions (8%), suggesting that most AE (microcrack) events were driven by the process of ice segregation rather than volumetric expansion. The outcomes of a novel statistical model of crack propagation based on two boundary conditions—inside–out and outside–in modes of cracking—were assessed based on Bayes’ theorem by testing the hypothesis that the inside–out mode of cracking was favoured by tensional activity, whereas the outside–in mode supported by shearing events. In both situations, the hypothesis accounted for 54–73% confidence level. The microcrack propagation model can distinguish reasonably between cracks formed by volumetric expansion and ice segregation.

1 **Experimental observations and statistical modelling of crack propagation dynamics**
2 **in limestone by acoustic emission analysis during freezing and thawing**

3 Vikram Maji^{1,2} and Julian B. Murton^{1,3}

4 ¹ Permafrost Laboratory, Department of Geography, University of Sussex, Brighton BN1 9QJ, UK

5 ² Experimental Rock Deformation Laboratory, Department of Earth Sciences, IIT Kanpur, Uttar
6 Pradesh- 208016, India

7 ³Corresponding author, email: j.b.murton@sussex.ac.uk; ORCID 0000-0002-9469-5856

8 Vikram Maji: email: vmaji@iitk.ac.in, V.Maji@sussex.ac.uk; ORCID [0000-0003-0870-6625](https://orcid.org/0000-0003-0870-6625)

9

10

11 **Key Points**

12 1. Most acoustic emissions occurred during thaw of a limestone block, consistent with
13 microcracking events due to ice segregation.

14 2. Microcracks propagating outward from the block centre favoured tensional cracking, whereas
15 those propagating inward favoured shearing events.

16 3. A new microcrack propagation model distinguishes reasonably between cracks formed by
17 volumetric expansion and ice segregation.

18 **Abstract**

19 The timing and location of microcracking events, their propagation and coalescence to form
20 macrocracks, and their development by tension, shearing or mixed modes are little known but
21 essential to understanding the fracture of intact rock by freezing and thawing. The aims of the
22 present study are to investigate the mechanisms and transition of micro- and macrocracking during
23 repeated freeze–thaw, and to develop a statistical model of crack propagation that assesses the

24 distance and angular relationship of neighbouring cracking events arranged in their temporal order
25 of occurrence. Eight acoustic emission (AE) sensors mounted on a 300 mm cubic block of chalk
26 captured the three-dimensional locations of microcracking events in their temporal order of
27 occurrence during 16 seasonal freeze–thaw cycles simulating an active layer above permafrost. AE
28 events occurred mostly during thawing periods (45%) and freeze-to-thaw transitions (37%) rather
29 than during freezing periods (9%) and thaw-to-freeze transitions (8%), suggesting that most AE
30 (microcrack) events were driven by the process of ice segregation rather than volumetric
31 expansion. The outcomes of a novel statistical model of crack propagation based on two boundary
32 conditions—inside–out and outside–in modes of cracking—were assessed based on Bayes’ theorem
33 by testing the hypothesis that the inside–out mode of cracking was favoured by tensional activity,
34 whereas the outside–in mode supported by shearing events. In both situations, the hypothesis
35 accounted for 54–73% confidence level. The microcrack propagation model can distinguish
36 reasonably between cracks formed by volumetric expansion and ice segregation.

37

38 **Plain language summary**

39 It is well known that repeated freezing and thawing of water within some porous and fine-grained
40 rocks can form large cracks visible to the unaided eye. But the initiation and growth of precursor
41 tiny cracks too small to see without a microscope remain enigmatic in terms of their timing,
42 location, growth and coalescence to form eventually large cracks. Thus, prediction of rock fracture
43 by frost is difficult. Here we present results from a laboratory experiment that measured the
44 location and timing of tiny sound (acoustic) waves within a block of limestone subject to 16 cycles
45 of freezing and thawing. The waves indicated the occurrence of tiny cracking events. Measurement
46 of rock temperature suggested that most cracking events resulted from water migrating through
47 the rock towards lenses of ice rather than expansion of water freezing in place within empty spaces

48 in rock. In addition, cracks propagating outward from the block centre tended to form as the rock
49 was being pulled apart, whereas those propagating inward tended to form by scissor-like tearing of
50 rock. A new statistical model of rock cracking can distinguish reasonably well between cracks
51 formed by growing ice lenses and those formed by expansion of freezing water.

52

53 **Keywords:** Acoustic emissions; freeze–thaw; crack propagation; ice segregation; permafrost

54 1. Introduction

55 Fracture of fine-grained, porous rock by initiation and growth of ice lenses is considered an
56 important mechanism of frost weathering ([Matsuoka and Murton, 2008](#)). This fracture process—
57 termed *ice segregation*—refers to migration of premelted water in liquid films through a porous
58 and permeable medium such as soil or rock towards freezing sites, where lenses or layers of ice
59 grow, segregated from adjacent mineral particles and aligned perpendicular to the temperature
60 gradient. Premelting occurs along ice–liquid interfaces, and it enables ice and liquid water to
61 remain in equilibrium at temperatures below 0°C ([Dash et al., 2006](#); [Rempel, 2011](#)). Migration of
62 premelted water results from suction induced by temperature gradients within porous media at
63 temperatures below 0°C. Freezing experiments under laboratory conditions indicate that
64 macrocracks can initiate and develop in intact rock, and fill with segregated ice ([Agakawa and](#)
65 [Fukuda, 1991](#); [Murton et al., 2006, 2016](#)). Less clear are: (1) When and where do the precursor
66 microcracks occur during different stages of freezing and thawing? (2) Do microcracks develop by
67 tension, shearing or mixed modes cracking? (3) How do microcracks propagate and coalesce to
68 form individual macrocracks and pervasively fractured (brecciated) horizons? We hypothesize that
69 tension, shearing and mixed modes of cracking activities of rock vary during different stages of

70 freezing and thawing. We address these questions by monitoring acoustic emissions (AEs)
71 generated by microcracking activity.

72 AEs are transient elastic waves produced by the rapid release of energy from localized sources
73 within a material. AE testing is a non-destructive method for investigating material behaviour based
74 on detection and conversion of high-frequency elastic waves into discrete electrical signals
75 ([Goszczyńska et al., 2014](#)). The transducer element in an AE sensor is a piezoelectric crystal that
76 responds with high sensitivity to motion in the low ultrasonic frequency range (10–2000 kHz).
77 When the AE wave front reaches the piezoelectric sensors mounted on the surfaces of a test
78 specimen, minute mechanical movements of the fracture surface molecules are sensed by the
79 transducer and converted to detectable electrical signal. The signal is then amplified and split into
80 discrete waveforms with characteristics such as amplitude, absolute energy, duration and rise time.
81 Multiple piezoelectric sensors arrayed around a structure allow the location of AE activity to be
82 estimated in three-dimensional (3-D) space, based on wave velocity within the material and
83 differences in hit arrival times among the sensors. AE activity has been measured in laboratory
84 freezing experiments with stable thermal boundary conditions ([Hallet et al., 1991](#); [Duca et al.,](#)
85 [2014](#)). Now it is timely to analyse the changes in AE under dynamic thermal boundary conditions
86 characteristic of natural freeze–thaw cycles.

87 Here we report observations of AE activity monitored during a laboratory experiment on freeze–
88 thaw of limestone. The rationale for the experiment is that 16 freeze–thaw cycles could be carried
89 out over a substantial period of time (470 days) in order to simulate multiple years of an active
90 layer above permafrost developed within a 300 mm cubic block of tuffeau, a type of chalk
91 (limestone) that readily fractures by ice segregation ([Murton et al., 2006](#)). Our aims are, first, to
92 investigate the mechanisms and transition of micro- and macrocracking during repeated freeze–
93 thaw, and, second, to develop a statistical model of crack propagation that assesses the distance

94 and angular relationship of neighbouring cracking events arranged in their temporal order of
95 occurrence. Our objectives are to (1) determine the 3-D location of individual cracking events
96 within the block using multiple AE sensors, and detect and analyze waveforms emitted during
97 them; (2) identify the spatial and temporal distribution, abundance and mechanical characteristics
98 of cracks during different stages of freezing and thawing; (3) distinguish between cracking modes I
99 (tension) and II (shear) during freeze–thaw cycling by parametric analysis of AE waveforms; (4)
100 construct two boundary conditions that reproduce different modes of crack propagation
101 (inside–outward and outside–inward); and (5) compare the patterns of fracture propagation using
102 Bayes’ theorem for the two boundary conditions with the tension and shear cracks observed using
103 AEs. The experimental set up and observations of macrocracks, temperature and strain are detailed
104 in a companion paper ([Maji and Murton, 2020a](#)) and the freeze–thaw regime is summarized below.

105 2. Methods

106 2.1 Freezing and thawing regime

107 The block of chalk was saturated by capillary rise before starting the experiment and also
108 between its four phases. The block initially froze downward from the top as a result of chilled air
109 circulating in a cold room. Once the block was frozen through, a cooling plate beneath the block
110 was turned on to maintain subzero temperatures in the lower part of the block (simulated
111 permafrost) for the remainder of the experiment. At intervals during the experiment, the chilled air
112 was turned off and the door of the cold room was opened to allow air at ambient room
113 temperature to circulate the cold room and thaw the upper part of the block from the surface
114 downward (simulated active layer). The temperature of the basal cooling plate was thermostatically
115 controlled, with the thermostat set at three progressively higher temperatures during four phases
116 of the experiment (P1–4) in order to simulate active-layer deepening and permafrost thaw during

117 16 freeze–thaw cycles. The values were set at -15°C for phase 1 (P1: cycles 1–4, days 0–68), -10°C
118 for P2 (cycles 5–8, days 69–203), and -5°C for both P3 (cycles 9–12, days 207–312) and P4 (cycles
119 13–16, days 315–470) (Figure 1a; Maji and Murton, 2020a). In summary, the experiment consisted
120 of 16 temperature cycles that simulated annual freeze–thaw of a deepening active layer above
121 permafrost.

122 Each freeze–thaw cycle was divided into four parts. (1) *Thaw-to-freeze transitions* represent the
123 time between imposing a sub-zero air temperature and the onset of more or less isothermal
124 conditions in the frozen chalk block. (2) *Freezing periods* represent the time between the onset of
125 more or less isothermal conditions in the frozen chalk block and the onset of an above-zero air
126 temperature. (3) *Freeze-to-thaw transitions* represent the time between turning off the chilled air
127 supply in the cold room and the development of a stable vertical temperature gradient in the
128 unfrozen simulated active layer. During these transitions the 0°C isotherm descended into the block
129 and stabilized at a certain depth, simulating progressive thaw of the active layer in summer. (4)
130 *Thawing periods* represent the time between the onset of a stable vertical temperature gradient in
131 the unfrozen simulated active layer and the onset of a sub-zero air temperature at the start of the
132 next thaw-to-freeze transition.

133 2.2 Acoustic emissions

134 2.2.1 Instrumentation, data acquisition and processing

135 Eight AE sensors (R-15 alpha, manufactured by Mistras Group) were mounted on five faces of
136 the chalk block (Figure 2). The sensors were distributed using a 3-D Cartesian co-ordinate system to
137 locate single cracking events. Two sensors were mounted diagonally on vertical faces A, B and C,
138 one on vertical face D, and one on the top horizontal surface (to monitor the depth of cracking). A
139 silicon grease epoxy (Pro silicone grease 494-124, from RS Components) was used to establish a

140 good contact between the smooth ceramic sensor face and the rough vertical rock surface, and a
141 metal cage secured the sensors in place during the experiment (Figure 2d). Two holes (3 mm
142 diameter, ~25 mm long) were drilled into the block to mount each cage, and plastic raw plugs
143 inserted into the holes to anchor the cage with screws. A screw on the top of the cage ensured that
144 the sensors were firmly pressed against the rock faces during the experiment.

145 The signal from each AE sensor was amplified by a 40 dB gain before processing. Each sensor
146 was connected by a cable 1.5 m long to a preamplifier (IL40S with 32–1100 kHz, Mistras Group)
147 placed inside a box in the cold room. The analog and digital filters used in the preamplifier had
148 ranges of 20–400 and 8–40 kHz, respectively. The preamplifiers were activated by a 28V DC
149 phantom power supply from a PCI Express-8 data card (Mistras Group) installed in a workstation
150 outside the cold room and connected to the preamplifiers by a 10-m-long BNC cable. The layout of
151 the AE data acquisition system is illustrated schematically in Figure 2a.

152 Data were processed using *AEWin 3D-LOC* software. A threshold of 40 dB was set to separate
153 noise induced in the laboratory from signals of microcracking events. The sampling rate was 1 MHz
154 and the values for peak definition time (PDT), hit definition time (HDT) and hit lockout time (HLT)
155 were 200, 800 and 1000 microseconds, respectively. Every hit captured by the sensors included the
156 parameters amplitude, energy, counts, duration, average signal level (ASL), rise time, average
157 frequency, signal strength and absolute energy.

158 An AE event was identified if at least four of the eight sensors captured the pulses of energy
159 released (hits). The number of hits and amplitude were considered to eliminate and filter out the
160 noise generated by the freezing system. Data acquisition was continuous throughout the
161 experiment, with a file of AE events produced every 12 hours.

162 2.2.2 Waveform characteristics

163 The waveform characteristics obtained from the acoustic waves included the number of hits,
164 duration of the signals, number of counts above a preset threshold (= 40 dB), rise time, amplitude,
165 and energy released (Figure 3a). In order to classify the nature of cracking, the RA value and
166 average frequency were calculated from the waveform characteristics as follows:

$$167 \text{ RA value} = \text{rise time} / \text{maximum amplitude} \quad (1)$$

$$168 \text{ Average frequency} = \text{AE counts} / \text{duration time} \quad (2)$$

169 These two parameters allowed cracks to be classified as mode I (tension) and mode II (shear) cracks
170 (Figure 3b; JCMS-IIIB5706, 2003; Ohno et al., 2010). The line separating tension and shear events
171 has a slope of 0.1 kHz ms/V following the convention used in JCMS-IIIB5706 (2003). Events lying on
172 the separation line are classified as mixed modes of cracking.

173 2.2.3 Three-dimensional (3-D) location detection principle

174 The 3-D locations of AE events were determined—with an additional plug-in code in the *AEWin*
175 software—from the differences in arrival time of acoustic waveforms at sensors that captured any
176 event. This code took into account the array of sensors around the block with respect to a fixed
177 Cartesian reference frame and the velocity of acoustic waves (longitudinal, shear and surface
178 waves) propagating through the material. Hits and events were classified based on their arrival
179 times at four or more sensors around the block. The acoustic wave velocity of the entire block was
180 assumed to remain constant throughout the experiment. This assumption is reasonable when the
181 rock was frozen (i.e., a during the middle to late stages of freezing periods), but during thawing
182 periods slight differences in acoustic wave velocity probably developed between the simulated
183 permafrost and active layer. The 3-D locations of the events within the block were visualized on a
184 graphical interface in *AEWin* and the information was stored for further analysis.

185 2.3 Statistical model

186 2.3.1 Theory and mathematical explanation

187 We developed a statistical model to assess the distance and angular relationships among the
188 temporal order of AE events. The model assumes that the locations and timings of cracking events
189 during the experiment relate to the crack initiation and propagation history observed in the chalk
190 block. The model measures the mean distance and mean angular relationship of the next specified
191 number (N) of consecutive events (N = 2, 5 and 10) relative to each event. The input, throughput
192 and output of the model are illustrated schematically in [Figure 4](#). The model is based on two
193 principal cases of fracture propagation and validated with the AE data recorded in the experiment.
194 The model depicts the best result when N=10, and so we considered N=10 for validation purposes.
195 The model considers the mechanism of crack propagation along the horizontal direction only,
196 because well-developed cracks observed in the block after 8, 12 and 16 freeze–thaw cycles were
197 dominantly horizontal. The model outcomes of the experimental results were correlated with the
198 parametric analysis of the AE waveforms in terms of tension, shear and mixed modes of cracking.
199 Bayesian statistical approaches were incorporated to validate the modelling outcomes on a
200 probability scale.

201 Two cases of fracture propagation were considered: (1) propagation of cracks from inside the
202 block outward toward the sides, i.e., inside–out ([Figure 5](#)), and (2) propagation of cracks from the
203 outer part of the block inward toward the centre, i.e., outside–in ([Figure 6](#)). Each case produced a
204 different set of 3-D points containing the locations of the events arranged according to their time of
205 occurrence. The fracture propagation model was then tested on the 3-D location matrices to
206 discriminate the patterns in both scenarios.

207 $\mathbb{E}n$ is the set containing information about the location of events arranged in their temporal
208 order during any sequence of cracking. It is defined as

209
$$\mathbb{E}n = \{\xi_1, \xi_2, \dots, \xi_n\} \quad (3)$$

210 where $\xi_1, \xi_2, \dots, \xi_n$ are the locations of cracking events and can be expressed as $\xi_n = [X_n, Y_n, Z_n]$. The
 211 fracture propagation mode $\mathbb{F}\mathbb{P}$ assesses the mean distance (r) and mean angular (θ) relationships
 212 of a predefined number ($N=2,5,10$) of next consecutive events and is defined as

213
$$\mathbb{F}\mathbb{P}(r) = f(\mathbb{E}n) \quad (4)$$

214
$$\mathbb{F}\mathbb{P}(\theta) = f(\mathbb{E}n) \quad (5)$$

215 Values of both $\mathbb{F}\mathbb{P}(r)$ and $\mathbb{F}\mathbb{P}(\theta)$ of the corresponding events that are far apart indicate events
 216 occurred at various locations within the block and can be interpreted as individual cracking events
 217 with no definite spatial relationship to each other. Conversely, values of $\mathbb{F}\mathbb{P}(r)$ of the
 218 corresponding events that are close together suggest spatially localized events and may indicate a
 219 sequence of cracking. This is true for both distance and angular relationships. $\mathbb{F}\mathbb{P}(\theta)$ was estimated
 220 by converting the location information $\xi_1, 2, \dots, \xi_n$ into a vector by joining them to the origin, and
 221 the angular relationship of events was derived using the dot product of location vectors.

222 2.3.2 Inside–out crack propagation

223 The inside–out propagation model assumes that a crack initiated inside the block and
 224 propagated outward towards the sides. To evaluate this mechanism against the brecciated layer
 225 observed in the experiment (Maji and Murton, 2020a), we considered a definite zone at a depth
 226 interval that generated a random set of 3-D numbers representing each AE event. The numbers
 227 were generated in order to simulate the inside–out propagation of a crack (Figure 5). As the crack
 228 lengthened, the spatial boundary condition of random number generation expanded on the either
 229 side, as visualized in Figure 5a. A total of 3000 random points was considered in ten consecutive
 230 segments, each with extended spatial boundary conditions relative to the previous one. The 3-D
 231 random numbers simulating AE events were restored in a set (\mathbb{E}_{i0}) according to their directional
 232 order of occurrence. The statistical model was then applied through the simulated event points,

233 and outcomes of both the angular and distance relationships are presented in [Figure 5b–c](#). The
234 nearest 2, 5 and 10 next consecutive events were considered while performing the statistical
235 algorithm at the initial model construction stage in order to assess the best possible outcome.
236 When the next number of consecutive events was lowest (N=2), the fluctuations in angular and
237 distance values were higher, and when the number was highest (N=10), the curve showed less
238 variation. Both the values of $\mathbb{F}\mathbb{P}_{10}(r)$ and $\mathbb{F}\mathbb{P}_{10}(\theta)$ followed a gently increasing trend ([Figure 5b–c](#)).

239 2.3.3 Outside–in crack propagation

240 The outside–in propagation model simulates a crack originating on two sides of the block within
241 a definite depth interval and propagating inward towards the middle. A similar protocol was
242 applied to create the set (\mathbb{E}_{OI}) of locations of events that replicates the outside–in propagation of
243 cracking ([Figure 6](#)). The distribution of random events that replicate \mathbb{E}_{IO} is illustrated in [Figure 6a](#).
244 Unlike the inside–out model, in the outside–in model, the results of the statistical algorithm for
245 both situations $\mathbb{F}\mathbb{P}_{OI}(r)$ and $\mathbb{F}\mathbb{P}_{OI}(\theta)$ followed a gently decreasing trend ([Figure 6b–c](#)).

246 2.3.4 Testing the model

247 Predicted $\mathbb{F}\mathbb{P}(r)$ and $\mathbb{F}\mathbb{P}(\theta)$ values of the statistical crack propagation model, developed by
248 considering the two distinct boundary conditions, were compared with the similar distance and
249 angular variations observed at different depth interval within the specimen during the physical
250 experiment. The observed hypocentres of AE events were spatially grouped into four depth
251 intervals determined from visual analysis of macrocracks and brecciation in the block after 16
252 freeze–thaw cycles, as described by [Maji and Murton \(2020a\)](#). The AEs in these depth intervals
253 were then filtered and arranged in their order of temporal occurrence following the time stamp
254 recorded during acquisition. The step processing structure of the fracture propagation function is
255 schematically illustrated in [Figure 4](#). The process was repeated for the each of the four depth
256 intervals.

257 3. Results

258 3.1 AE activity

259

260 AE activity during the four parts of a representative freeze–thaw cycle (freezing period, freeze-
261 to-thaw transition, thawing period and thaw-to-freeze transition) is exemplified from freeze–thaw
262 cycle 5 (Figure 7). The full set of AE activities recorded during all 16 cycles is shown in Supporting
263 Figures S1–S20 and summarized below in terms of their constituent parts.

264 3.1.1 Freezing periods

265 Freezing periods had an average duration and standard deviation of 12.68 ± 7.25 days and
266 encompassed 9.46 % of the total number of AE events. AE events were recorded mostly during
267 freezing periods (F) 3–5, with few events during F10 (Table 1; Figures S1–S2). F3–5 occurred during
268 phases P1 and early P2, when the temperature of the air and basal cooling plate was relatively low
269 (Maji and Murton, 2020a).

270 AE activity clustered mostly around face A during F3–5, with limited clustering around faces C
271 and D (Figure S1: panels 1–4). High-amplitude events (>64 dB) occurred around face A. F10
272 experienced relatively few events compared to F3–5. In F10, AEs occurred near face B and in the
273 central part throughout the depth of the block, with moderate- to high-magnitude events (56–72
274 dB) around face B. Moderate- to high-amplitude events were most abundant in the 180–300 mm
275 depth range, although some low-amplitude events (<48 dB) occurred in the upper half of the block
276 (Figure S2: panels 1–4). In F3 and F10, AEs occurred within a short window of time, whereas in F4–
277 5, they continued throughout the freezing period (Figure S1: panels 5–12). In F3–5, the number and
278 magnitude of shearing mode events were higher than those of tension, whereas F10 was
279 dominated by tension mode events (Figure S2: panels 5–12). Overall, comparatively steep freezing

280 gradients during P1 initiated AE activity near the beginning of the experiment, and as the intensity
281 of freezing fell in later cycles, the frequency of AE activity reduced.

282 3.1.2 Freeze-to-thaw transitions

283 Freeze-to-thaw (FT) transitions had a mean duration of 1.5 ± 0.17 days and encompassed
284 36.98% of the total number of AE events. Substantial AE activity occurred during all 16 FT
285 transitions (Figures S3–S8; Table 2).

286 In P1, when the thermal gradient was highest, AE events occurred mostly in the lower half of
287 the block (Figure S3: panels 1–4). In FT1, AEs were mostly in the central part of the block, but in
288 FT2–4, they were mostly near vertical faces A and C (Figure S4: panels 1–4). Some moderate- to
289 high-amplitude (64–80 dB) activity occurred during FT1–2 (Figures S5 and S6: panels 1–4). The
290 tension mode of cracking dominated over the shearing mode, and the intensity of shearing
291 gradually decreased during the course of P1 (Figures S7 and S8: panels 1–4).

292 In P2–3, when the basal thermal protocol was moderate (-10°C compared to -15°C in P1), the
293 modal depth of the frequency distribution of AE events moved upward into the middle of the block
294 (Figure S3: panels 5–12). However, at the onset of restarting the experiment after pauses between
295 P1 and P2, and between P2 and P3, AE activity was concentrated in the lower half of the block,
296 which is also evident in the transition between P3 to P4 (Figure S3: panels 5, 9 and 13). AE events in
297 P2–3 were mostly localized within the block, unlike the clustering of AEs around the faces observed
298 in P1 (Figure S4: panels 5 and 12). Moderate- to high-magnitude events (56–72 dB) were prevalent,
299 though the high amplitudes clustered mostly around the faces. New clustering of events around
300 faces were marked by high-amplitude activity, as observed in FT 1–2 near face A and in FT 9–10
301 around face B (Figure S4). High-magnitude activity (> 72 dB) was bounded by initiation and follow-
302 up events both in the depth and time domain, as observed in FT1, 2, 6, 10, 11, 13 and 15 (Figures S5

303 and S6). The magnitude of shearing events increased in P2–3, though both tension and shearing
304 modes were abundant (Figures S7 and S8).

305 In P4, AE events occurred throughout the depth of the block and moderate to high-amplitude
306 events were evident (Figure S3: panels 13–16). Both tension and shear modes were abundant.

307 In summary, intense bidirectional freezing coincided with AE activity concentrated in the lower
308 half during P1, whereas higher temperatures in P2–3 coincided with modal AE activity in the central
309 parts of the block. In addition, AEs were localized within the block rather than clustered around
310 faces, though high-magnitude events were localized around faces during P2–3.

311 3.1.3 Thawing periods

312 Thawing periods (T) had an average duration of 13.81 ± 5.38 days and encompassed more AE
313 events (45.37%) than any other parts of the freeze–thaw cycles (Figures S9–S14; Table 3).
314 However, no activity was recorded in T9 and 15.

315 In P1, AE activity mostly occurred in the lower half of the block (Figure S9). The events were
316 highly clustered and isolated around the faces A and C (Figure S10). High-amplitude events (64–72
317 dB) occurred in the upper half of the block (Figures S11–S12). During the entire thawing periods,
318 the tension mode of cracking was of higher magnitude than that of shearing mode. Also, the
319 number of tension events was higher than shearing.

320 In P2–3, the modal depth of AE activity moved higher within the block, similar to that in FT
321 transitions (Figure S9). In addition, abundant events occurred within the block, connecting the
322 clusters developed near the faces during P1 (Figure S10). Faces A and C were mostly connected
323 during P2, whereas faces B and D were bridged in P3. Moderate- to high-amplitude events (56–72
324 dB) occurred in the central and lower parts of the block (Figures S11–S12).

325 In P4, AE events occurred in the middle and lower parts of the block (Figure S10). Clustering of
326 AE occurred around faces, mostly near face D and particularly in the upper half of the block (Figure

327 S10). Low- to moderate-magnitude events (56–72 dB) occurred in P4 and were concentrated in the
328 middle to lower half of the block (Figures S11–S12).

329 Overall, high-amplitude events (70–80 dB) were fewer in thawing periods than in freeze-to-
330 thaw transitions. The tension activity was most abundant within the 30–40 (average frequency) kHz
331 window in thaw cycles as compared to freeze-to-thaw transitions, where < 30 kHz events were also
332 recorded. In contrast, freeze-to-thaw transitions recorded higher magnitude shear events than
333 thawing periods (Figures S13–S14).

334 3.1.4 Thaw-to-freeze transitions

335 Thaw-to-freeze (TF) transitions had a mean duration of 1.5 ± 0.71 days and encompassed only
336 ~8.17% of the total number of AE events (Figures S15–S20; Table 4). AE activity was greatest in P1–
337 2. Six transitions (TF 1, 6, 10–12 and 16) lacked any AE events.

338 During P1–2, AE activity occurred mostly in the lower half of the block, whereas in P3–4 very
339 few events were identified (Figure S15). Events mostly clustered around faces A and C, with limited
340 numbers of AEs occurring in the central part of the block (Figure S16). Medium- to high-amplitude
341 events (56–72 dB) were observed in TF2 at ~100–250 mm depth, whereas the rest of the activities
342 were of low to medium amplitude (40–56 dB) (Figures S17 and S19). Both tensional and shearing
343 modes of cracking occurred, with some shearing mode events of high magnitude (Figures S18 and
344 S20).

345 3.1.5 Summary

346 Most AE events occurred during thawing periods (~45%) and freeze-to-thaw transitions (~37%),
347 with fewer in freezing periods (~9%) and thaw-to-freeze transitions (~8%). In terms of depth, all AEs
348 (>40 dB), including those of higher magnitude (>60 dB), were concentrated mostly in the lower half
349 of the block in P1, but the modal depth of the events moved upward in P2–3, and events were
350 distributed throughout the block in P4 (Figure 8). In terms of 3-D location, AEs were mostly

351 clustered and isolated around faces A and C in P1. In P2–4, events were observed in the central part
352 of the block connecting the clusters. However, some new clusters developed around faces B and D
353 during P3 and P4. In terms of magnitude, most events were low to moderate amplitude, though
354 moderate- to high-amplitude events were abundant during P1–3. The modes of cracking were
355 mostly tensional, though abundant shearing activities were recorded. The magnitude of tensional
356 activity was highest in thawing periods. In some instances, however, the magnitude of shearing
357 modes was relatively high in freeze-to-thaw and thaw-to-freeze transitions.

358 3.2 Crack propagation models at different depth intervals

359 The experiment formed visible macrocracks at four different depth intervals in the block. These
360 comprise two brecciated horizons at depths of 70–110 mm and 180–220 mm and two horizons with
361 limited numbers of inclined macrocracks at depths of 0–60 mm and 120–170 mm (Figure 9). The
362 brecciated horizons contained mostly horizontal to subhorizontal macrocracks that bifurcated and
363 joined, separating angular and tabular fragments of chalk, and cross-cut by fewer vertical to steeply
364 dipping macrocracks. The lightly cracked horizons above and between the brecciated horizons
365 consisted of single to a few cracks, mostly horizontal to subhorizontal. Further details of the
366 macrocracks are given by Maji and Murton (2020a). First, we describe the timing of aggregated AE
367 events at different depth intervals during the four thermal phases of the experiment, and then we
368 examine the crack propagation models at these different depths.

369 3.2.1 AE timing during phases 1–4

370 The timing of AE events in the four depth horizons varied with the imposed thermal boundary
371 conditions (basal cooling thermostat values of -15°C for P1, -10°C for P2, and -5°C for both P3 and
372 P4; Figure 1a). AE events were most abundant in the upper brecciated horizon (70–110 mm depth)
373 during P2–4 ($n=273\text{--}338$) and least abundant in P1 ($n=193$), when the temperature was lowest
374 (Figure 10). Conversely, events were most abundant in the lower brecciated horizon (180–220 mm

375 depth) during P1–2 (n=2087–2449), and less common in P3–4 (n=503–828) (Figure 11). In
 376 comparison, AEs were most common in the upper horizon of limited fracture (0–60 mm depth)
 377 during P3–4 (n=158–273), and less common in P1–2 (n=89–94) (Figure 12). Finally, AEs in the lower
 378 horizon of limited fracture (120–170 mm depth) were most common in P2 (n=1507) and least
 379 common in P1 and P3–4 (n=437–693) (Figure 13).

380 3.2.2 Brecciated horizons

381 Both brecciated horizons decreased overall in the values of $\mathbb{F}P(r)$ and $\mathbb{F}P(\theta)$ during the
 382 experiment, especially during the first phase (P1). In P1, $\mathbb{F}P(r)$ decreased from ~ 160 to ~ 80 mm at
 383 70–110 mm depth (Figure 10b) and from ~ 180 to ~ 50 mm at 180–220 mm depth (Figure 11b).
 384 Respective drops in $\mathbb{F}P(\theta)$ in P1 were from ~ 50 to $\sim 30^\circ$ (Figure 10b) and from ~ 50 to $\sim 20^\circ$ (Figure
 385 11b). The transition between P1 and P2 marked with a sharp increase in both $\mathbb{F}P(r)$ and $\mathbb{F}P(\theta)$,
 386 whereas, the values continued to decrease during P2 in both the brecciated horizons (Figures 10b
 387 and 11b). Both parameters tended to fluctuate, sometimes substantially, during P3–4, where the
 388 amount of oscillation surpassed the overall trend. The highest number of AE events was observed
 389 at 180–220 mm depth. AE activity was particularly common during thawing periods and FT
 390 transitions in P1–2, though substantial activity also occurred during freezing periods in P1, when
 391 the thermal boundary condition was at its lowest (Figures 10c and 11c). At both depth intervals, the
 392 majority of cracking events were of shearing mode in P1 and P2, and of tensional mode in P3 and
 393 P4 (Figures 10a and 11a).

394 3.2.3 Horizons of limited fracture

395 AE activity was least within the shallow horizon of limited fracture (0–60 mm depth, Figure
 396 12), whereas the deeper horizon of limited fracture (120–170 mm depth) showed the second
 397 highest AE activity (Figure 13). During P1–2, the values of $\mathbb{F}P(r)$ and $\mathbb{F}P(\theta)$ declined overall at
 398 120–170 mm depth (Figure 13b), whereas no obvious trends occurred in either parameter at 0–60

399 mm depth (Figure 12b). The maximum fluctuation in $\mathbb{F}\mathbb{P}(r)$ and $\mathbb{F}\mathbb{P}(\theta)$ at 120–170 mm depth
400 corresponds to 140 mm and 32°, respectively (~190 to ~50 mm and 47–15°) and 40 mm and 40°
401 (~80 to ~40 mm and 50–10°), and at 0–60 mm depth to 60 mm and 16° (~150 to 90 mm and
402 33–17°) and 90 mm and 45° (~200 to ~110 mm and 50–5°) during P1–2. During P3–4 the overall
403 changes in both the values of $\mathbb{F}\mathbb{P}(r)$ and $\mathbb{F}\mathbb{P}(\theta)$ were low at both the depth intervals (Figures 12–
404 13b), and both parameters experienced occasional variation, sometimes substantial. The AE events
405 occurred mostly during the freezing periods in P1 and during thawing periods in P2. In contrast, the
406 events were mostly developed during thawing periods followed by FT transitions in the upper
407 horizon during P3–4, whereas the order was reversed (i.e., FT transitions followed by thawing
408 periods) in the lower horizon. The majority of fracturing activity was of shearing mode in P1 and
409 tension mode in P2–4 (Figures 12–13a).

410 4. Discussion

411 No additional mechanical loading was imposed during the experiment and the fractures
412 developed purely under dynamic thermal boundary conditions. Cracking of rocks under repeated
413 freezing and thawing tends to be slower than that under mechanical loading, and so a long
414 experiment (470 days) with 16 freeze–thaw cycles was required to produce well-developed crack
415 surfaces in a relatively soft limestone. The slow development of cracks—monitored using AEs—
416 elucidates the timing of AEs during freeze–thaw cycles, the depth of AEs and macrocracks, and the
417 modes and mechanisms of cracking. In turn, this permits evaluation of a new statistical model of
418 crack propagation and assessment of the practical significance of distinguishing between cracks
419 formed by volumetric expansion and ice segregation.

420 4.1 Timing of AE events during freeze–thaw cycles

421 The timing of AE events within the four parts of each freeze–thaw cycle suggests that the
422 majority of AEs did not result from microcracks formed by volumetric expansion but instead from
423 ice segregation. The maximum number of AE events (45.37%) occurred during thawing periods,
424 followed by freeze-to-thaw transitions (36.98%), even though the average duration of the
425 transitions was only 1.5 days. The fewest AE events were observed during freezing periods (9.46%)
426 and thaw-to-freeze transitions (8.17%). Collectively, this timing suggests that the large majority
427 (>82%) of microcracking events was not associated with rock freezing but instead with rock thawing
428 (during the earlier stages of thawing periods and during freeze-to-thaw transitions) or unchanging
429 thermal conditions (during the later stages of thawing periods). Therefore, we discount volumetric
430 expansion—which is predicted to occur in bursts during rock freezing, as liquid water freezes and
431 expands (Walder and Hallet, 1986)—as the main cause of AEs. We conclude that most AEs resulted
432 from ice segregation. The process of ice segregation is expected when temperature-gradient-
433 induced cryosuction draws liquid water to ice bodies within cracks (Taber, 1930; Walder and Hallet,
434 1986), which may arise as rock thaws or freezes. However, we cannot discount volumetric
435 expansion as a cause of AEs during freezing periods or thaw-to-freeze transitions. For example, in
436 freezing periods, AE activity was mostly limited to P1, which implies that for the lowest basal
437 temperature regime (i.e., -15°C and lower), AEs were caused by volumetric expansion as the low
438 temperature led to rapid freezing of pore water within the chalk. Freezing of pore water may have
439 been caused by either rapid cooling downward from the rock top and/or upward from the
440 simulated permafrost, which may explain the depth distribution of AEs shown in Figures 8 and S2:
441 F3–F5.

442 The timing of AE activity under laboratory conditions may be compared with that reported under
443 field conditions. At 3500 m above sea level in the Swiss Alps, AE activity and rock temperature

444 monitored during the course of four days in a south-facing alpine rockwall formed of granitic gneiss
445 revealed that AE activity increased significantly when rock temperature was $<0^{\circ}\text{C}$, especially at
446 locations receiving meltwater from snow (Armitrano et al., 2012). Rock at 10 cm depth warmed to
447 10°C during the day and cooled to -5°C during night, while rock at 60 cm depth remained
448 continuously between about -2° to -7°C . The increased AE activity during periods of sub-zero
449 temperature, when near-surface rock experienced refreezing, suggested that freezing-induced
450 stresses contributed to rock damage. Subsequently, AE monitoring at this location for a period of
451 one year showed that rates of AE energy detected during freezing conditions were about two
452 orders of magnitude greater than those under thawed conditions, suggesting that freezing-induced
453 processes largely accounted for AE activity (Girard et al., 2013). AE activity during freezing periods
454 ranged over temperatures from just below 0°C —which might indicate in situ freezing and
455 volumetric expansion—down to as low as -15°C —consistent with water migration and ice
456 segregation. A major difference between the field site and our laboratory experiment is rock
457 porosity: the interjoint porosity of the granitic gneiss (1–2 %) is far lower than that of the tuffeau
458 ($\sim 47\%$; Murton et al., 2000). Thus, it is to be expected that the intact bodies of gneiss between
459 fractures will be much less susceptible to migration of liquid water and resultant ice segregation
460 than the tuffeau. At a rock slope developed in conglomerate in Austria, some AE activity coincided
461 with freeze–thaw temperature cycles, and has been linked to observed detachment of boulders
462 from the slope (Codeglia et al., 2017).

463 4.2 Depth of AE events and macrocracks

464 The depth of AE events during phases 1 to 4 of the experiment (Figure 8) shows only limited
465 correspondence to the depth of macrocracks observed after phases 2, 3 and 4 (Figure 9). In phase 1
466 the majority of AEs—both in terms of total number and high magnitude (>60 dB)—were

467 concentrated below 180 mm depth, peaking between 250 and 300 mm depth (Figure 8a and e). In
468 phase 2 the modal depth decreased to ~190–260 mm (Figure 8b and f), whereas in phases 3 and 4
469 AEs were more uniformly distributed with depth (Figure 8c, d, g and h). Macrocrack development,
470 by contrast, was observed to form a brecciated horizon initially at 70–110 mm depth by the end of
471 phase 2 (Figure 9a), followed by a second, deeper brecciated horizon at 180–220 mm depth during
472 phases 3 and 4 (Figure 9b and c). The increase in depth of brecciation during the experiment has
473 been attributed to overall deepening of the simulated active layer above permafrost between
474 phases 1 and 4 (Figure 1a; Maji and Murton, 2020a).

475 The limited correspondence between the depths of AE events and macrocracks is attributed
476 tentatively to three factors. First, the abundant AEs recorded in the basal part of the block during
477 phase 1 were mostly of low amplitude (40–50 dB; Figure S1) and may be explained by the low
478 temperature protocol followed at the base. Such AEs did not lead to any observed macrocracks,
479 possibly because many AEs resulted from volumetric expansion within the pores during freezing
480 periods and thaw-to-freeze transitions. Second, some vertical to subvertical macrocracks developed
481 in the chalk, indicating that macrocrack development was not confined to the two brecciated
482 horizons but was more widely distributed in the block. Such cracks may function as conduits for
483 migration of unfrozen water towards the freezing front to facilitate ice segregation (Fukuda, 1983;
484 Maji and Murton, 2020a). Third, the number of AEs decreased overall during the course of the
485 experiment (Figure 8), consistent with reduced amounts of AE activity with increasing numbers of
486 freeze–thaw cycles reported in experiments on concrete (Todak et al., 2017) and granite (Wang et
487 al., 2019). This progressive reduction in AE activity probably resulted, at least in part, from
488 increasing heterogeneity in the chalk, as the macrocracks propagated. Increasing heterogeneity as
489 the rock fractured likely caused increasing attenuation of the AE signal (cf. Weber et al., 2018),
490 which may have limited the number of AEs registered by the sensors around the block.

491 4.3 Mechanisms and modes of cracking

492 Mechanistically, ice segregation alone may have caused microcracking during thawing periods
493 and freeze-to-thaw transitions, but we discount volumetric expansion at such times as a cause
494 because phase change from liquid water to ice requires rock cooling and freezing. However, both
495 ice segregation and/or volumetric expansion may have caused microcracking during freezing
496 periods and thaw-to-freeze transitions.

497 Moderate- to high-amplitude (64–80 dB) AE activity during freeze-to-thaw transitions was
498 observed as clusters near faces A and C early in the experiment, suggesting that development of
499 new clusters was facilitated at the face boundaries, followed by high-magnitude events (>70 dB). In
500 phase 1 (i.e., lowest thermal boundary conditions; [Figure 1a](#)), the dominant low-magnitude tension
501 mode of cracking suggests that the microcracks were caused by volumetric expansion mostly during
502 freezing periods and thaw-to-freeze transitions as the chances of well-developed lenses of
503 segregated ice were minimal in the early phases of the experiment. By contrast, AE events during
504 thawing periods in P1 were mostly isolated near the face boundaries ([Figure S10: panels 1–4](#)),
505 whereas in freeze-to-thaw transitions, some events occurred within the block ([Figure S4: panels](#)
506 [1–4](#)), which suggests that melting of ice initiated events within the well-developed clusters near the
507 face boundaries. Also, high-amplitude events in the upper half of the block during thawing periods
508 in P1 correlate with the well-developed brecciated layer at ~70–110 mm depth.

509 In P2–3, moderate- to high-amplitude events (56–72 dB) occurred within the block, implying
510 that warmer thermal boundary conditions were suitable for developing segregated ice lenses.
511 However, the clustering of high-magnitude activity near the faces suggests that surface boundaries
512 are weaker zones for initiation of ice lenses than within the block due to the differences in
513 confining pressure, as high pressure favours melting of ice even if the temperature gradient
514 remains identical. In addition, the magnitude of shearing events increased in P2–3, which is

515 interpreted to indicate the coalescence of microcracks into developing macrocracks. Specifically, ice
516 segregation was facilitated as the basal temperature conditions increased and the time duration
517 was enhanced in P2–3 than in P1 and corresponds with crack coalescence by connecting isolated
518 clusters developed in P1, as evident by the well-developed brecciated layers at depths from ~100
519 mm to ~200 mm.

520 In thawing periods, the tension activity was most abundant within the 30–40 kHz window
521 (Figure S13–S14) compared to freeze-to-thaw transitions, where <30 kHz events were also recorded
522 (Figure S7–S8). During thawing periods the temperature gradient allows for the development of
523 segregated ice within the pre-existing cracks and voids that open up the cracks in tension mode.
524 Depending on the size of the segregated ice lenses, the magnitude of tension events varied and in
525 the case of thawing comparatively higher magnitude activity was recorded. In contrast, freeze-to-
526 thaw transitions recorded higher magnitude shear events than thawing periods (Figures S8 and
527 S14). We hypothesize that in freeze-to-thaw transitions, partial melting of ice crystals formed
528 during freezing periods begins and the premelting layer of water acts as a slip surface for fracture
529 to slide one after another, causing relatively high-magnitude shearing activity observed in freeze-
530 to-thaw transitions.

531 4.4 Statistical modelling of crack propagation

532 Maji and Murton (2020b) classified different zones of microcracking based on micro-computed
533 tomography (μ -CT) analysis of 20 freeze–thaw cycles of a cylindrical core of the same chalk lithology
534 (30 mm long, 20 mm diameter). However, the mechanisms of crack propagation were not
535 identified. For the statistical model of crack propagation proposed in the present study, the results
536 of the hypothetical simulation were compared with the experimental results. The relationships
537 between the proposed mechanisms of crack propagation (inside–out and outside–in) and the

538 modes of cracking (tension, shear and mixed) are summarised in a Venn diagram (Figure 14). It is
539 evident that each mode of propagation consists of cracks of tension, shear and mixed modes of
540 origin.

541 Probabilistic assessment of the experimental results based on Bayes' theorem is summarised in
542 Table 5 for the four parts of each freeze–thaw cycle (freezing period, freeze-to-thaw transition,
543 thawing period and thaw-to-freeze transition). For each part, the probability of occurrences of any
544 particular type of event was assessed based on prior knowledge related to the prevalence of that
545 event. Column two represents the probability of occurrences of tension events provided that the
546 inside-out mode of propagation had occurred as a related background condition. The reverse
547 scenario is represented in column three, where the probability of the inside-out mode of
548 propagation is evaluated following the prior correlated condition assuming that the tension mode
549 of cracking had taken place. Column four illustrates the probability of occurrences of shearing
550 events following the condition that the outside-in mode of propagation has occurred. Column five
551 documents the opposite situation, evaluating the probability of outside-in events when shearing
552 modes of cracking existed. Overall, we tested the hypothesis that the inside–out mode of crack
553 propagation (i.e., increasing FIP) is facilitated by tensional cracks, whereas the outside–in mode is
554 assisted by shearing cracks (i.e., decreasing FIP). The hypothesis is supported by 54% (minimum) to
555 73% (maximum) confidence level, with an average of 64.88% for various parts of freeze–thaw
556 cycles.

557 Acceptance of the hypothesis suggests that the inside-out and outside-in approach of
558 quantifying the fracture propagation method—based on statistical modelling of the crack
559 propagation dynamics—was influenced to some extent by the modes of cracking (tension, shearing,
560 and mixed). By implication, the growth of any crack that develops under such dynamic thermal
561 boundary conditions can be broadly predicted.

562 4.5 Application of crack propagation model for isolating volumetric expansion and ice 563 segregation mechanisms

564 The negative trends for both $\mathbb{F}^{\mathbb{P}}(r)$ and $\mathbb{F}^{\mathbb{P}}(\theta)$ were relatively steep in P1 compared to other
565 phases, and contained short episodes of increase (Figures 10–13). Some episodes of tensional
566 activity attributed to volumetric expansion formed at various locations throughout the depth
567 window, and started to interact with each other, as indicated by the sharp decreases in $\mathbb{F}^{\mathbb{P}}(r)$ and
568 $\mathbb{F}^{\mathbb{P}}(\theta)$. In P2, when the thermal protocol was higher than P1, the slope of the negative trend
569 reduced, and the episodic spikes in positive trend increased. The increases were of steep slope,
570 suggesting potential tensional events attributed to ice segregation that may have allowed growth of
571 thicker ice lenses as compared to volumetric expansion when an extreme thermal protocol was
572 established. Similar mechanisms were inferred during P3 as well when the temperature protocols
573 were identical with that of P2 except some high-magnitude spikes. Similar repeated spikes occurred
574 in P4, when the temperature at the bottom of the block was highest. Such spikes were correlated
575 with the hypothesized thicker ice lenses as thermal protocols and duration of freezing and thawing
576 cycles were highest, favouring ice segregation. This also correlated with the brecciated horizon at
577 ~70–110 mm depth that was partially formed after 8 FT cycles but well developed after 16 cycles.

578 4.6 Limitations and recommendations for future research

579 The present study investigated the applicability of using AEs as a non-destructive method
580 during rock freezing and thawing for an order of magnitude longer duration than previous
581 experiments (Hallet et al., 1991; Duca et al., 2014) and, for the first time, during dynamic thermal
582 conditions. However, some limitations of our experiment are apparent.

583 First, the dynamic thermal boundary conditions around the chalk block imposed a vertical
584 thermal gradient, causing the lower part to remain frozen during most of the experiment, while the
585 upper part experienced repeated freeze–thaw. We assumed a uniform AE wave velocity

586 throughout for detecting the 3D locations of the micro- and macrocracking events, although the
587 variation in temperature changes the consistent attenuation of the AE wave velocities.

588 Second, deformation-induced heterogeneity was excluded in the present study. However, it
589 was observed that the degree of deformation controls the waveform attenuation to a certain
590 extent. The intact specimen at the beginning of the experiment showed a steady value of
591 attenuation and the wave velocity may have varied through time as the material developed
592 brecciated horizons and other macrocracks.

593 In view of both limitations, we therefore recommend that future experiments consider the
594 temperature- and deformation-induced changes in AE wave velocities for precisely locating the
595 cracking events in 3D as these two factors influence the attenuation of AE waveforms.

596 5. Conclusions

597 The following conclusions are drawn from the present study:

- 598 1. AE events occurred mostly during thawing periods (45%) and freeze-to-thaw transitions (37%)
599 rather than during freezing periods (9%) and thaw-to-freeze transitions (8%). This observation
600 supports the hypothesis that the majority of AE activity was associated with rock fracture
601 caused by ice segregation rather than volumetric expansion.
- 602 2. The modal depths of AE events were poorly correlated with the depths of macrocracks that
603 comprised two brecciated horizons. Possibly, the low-magnitude AE events have limited
604 influence on developing the brecciated horizons.
- 605 3. Early phases of the experiment revealed significant AE activity around the vertical faces of the
606 block, whereas later phases had high-magnitude events within it. This suggests that face
607 boundaries are weaker regions where microcracking initiated, compared to interior regions. We

608 hypothesize that lower confining pressure around the faces facilitates stable growth of ice
609 crystals.

610 4. Phase one of the experiment—with lowest basal temperature protocol (-15°C)—was dominated
611 by tension mode microcracking, which suggests that the lowest temperatures initiated
612 volumetric expansion. Higher basal temperature protocols in phases 2 (-10°C) and 3 (-5°C) were
613 associated with shearing events, allowing stable growth of ice lenses developed mainly by ice
614 segregation. The magnitude of tension mode cracking was higher during thawing periods,
615 facilitating development of ice lenses. By contrast, the occurrence of high-magnitude shearing
616 events mostly during freeze-to-thaw transitions is hypothesized to indicate that partial melting
617 of ice provided slip surfaces (of low friction) for fractures to slide over the thin film of premelted
618 water.

619 5. Microcrack propagation from inside the block towards the outside (inside-out mode) favoured
620 tensional cracking, whereas propagation from the outer part of the block towards the interior
621 (outside-in mode) favoured shearing events.

622 6. The proposed microcrack propagation model can distinguish reasonably between cracks formed
623 by volumetric expansion and ice segregation, based on the slope of the probabilistic values
624 connecting the distance and angular relationships of corresponding events.

625 Acknowledgements

626 This research is part of the senior author's doctoral research at the University of Sussex. The
627 research was funded by a Chancellor's international research scholarship and a Global Studies
628 studentship in the Department of Geography. Tim Cane provided help and guidance with
629 experimental design, sample preparation and use of equipment in the Permafrost Laboratory. Rhys
630 Pullin and Matthew Pearson (Institute of Mechanical and Manufacturing Engineering, Cardiff

631 University) provided guidance about acoustic emissions and access to rock testing apparatus.
 632 Marcus Dodds, Ed Haslam and Russell Swift (British Geological Survey, Keyworth) provided advice
 633 about acoustic emissions. Peter Cleall (Cardiff University) and John Barlow (University of Sussex) are
 634 thanked for comments on an earlier version of the manuscript.

635 Data availability statement

636 The dataset for this research is available from the University of Sussex Research Data Repository
 637 <https://doi.org/10.25377/sussex.14040029>

638 Private link for review purposes: <https://figshare.com/s/84dc99c3ed21a9e8597e>

639 References

- 640 Akagawa, S., & Fukuda, M. (1991). Frost heave mechanism in welded tuff. *Permafrost and*
 641 *Periglacial Processes*, 2(4), 301–309. <https://doi.org/10.1002/ppp.3430020405>
- 642 Armitrano, D., Gruber, S., & Girard, L. (2012). Evidence of frost-cracking inferred from acoustic
 643 emissions in a high-alpine rock-wall. *Earth and Planetary Science Letters*, 341–344, 86–93.
 644 <https://doi.org/10.1016/j.epsl.2012.06.014>
- 645 Azmatch, T. F., Arenson, L. U., & Segó, D. C. (2008). Measuring ice lens growth and development of
 646 soil strains during frost penetration using particle image velocimetry (GeoPIV). In Kane DL, Hinkel
 647 KM. (Eds.), *Proceedings of the 9th International Permafrost Conference, 29 June–3 July 2008,*
 648 *University of Alaska Fairbanks.* (Vol. 1, pp. 89–93). Fairbanks: Institute of Northern Engineering,
 649 University of Alaska Fairbanks.
- 650 Ballantyne, C. K. (2018). *Periglacial Geomorphology*. Chichester: Wiley.
- 651 Codeglia, D., Dixon, N., Fowmes, G. J., & Marcato, G. (2017). Analysis of acoustic emission patterns
 652 for monitoring of rock slope deformation mechanisms. *Engineering Geology*, 219, 21–31.
 653 <https://doi.org/10.1016/j.enggeo.2016.11.021>

- 654 Dash, J. G., Rempel, A. W., & Wettlaufer, J. S. (2006). The physics of premelted ice and its
655 geophysical consequences. *Reviews of Modern Physics*, 78(3), 695–741.
656 <https://doi.org/10.1103/RevModPhys.78.695>
- 657 Duca, S., Occhiena, C., Mattone, M., Sambuelli, L., & Scavia, C. (2014). Feasibility of ice segregation
658 location by acoustic emission detection: a laboratory test in gneiss. *Permafrost and Periglacial*
659 *Processes*, 25(3), 208–219. <https://doi.org/10.1002/ppp.1814>
- 660 Fukuda, M. (1983). The pore water pressure in porous rocks during freezing. In *Proceedings of the*
661 *Fourth International Conference on Permafrost, 17-22 July, Fairbanks, Alaska*. (pp. 322–337).
662 Washington, DC: National Academy of Sciences.
- 663 Girard, L., Gruber, S., Weber, S., & Beutel, J. (2013). Environmental controls of frost cracking
664 revealed through in situ acoustic emission measurements in steep bedrock. *Geophysical*
665 *Research Letters*, 40(9), 1748–1753. <https://doi.org/10.1002/grl.50384>
- 666 Goszczyńska, B. (2014). Analysis of the process of crack initiation and evolution in concrete with
667 acoustic emission testing. *Archives of Civil and Mechanical Engineering*, 14(1), 134–143.
668 <https://doi.org/10.1016/j.acme.2013.06.002>
- 669 Hall K. (1999). The role of thermal stress fatigue in the breakdown of rock in cold regions.
670 *Geomorphology*, 31(1–4), 47–63. [https://doi.org/10.1016/S0169-555X\(99\)00072-0](https://doi.org/10.1016/S0169-555X(99)00072-0)
- 671 Hallet, B., Walder, J. S., & Stubbs, C. W. (1991). Weathering by segregation ice growth in
672 microcracks at sustained sub-zero temperatures: verification from an experimental study using
673 acoustic emissions. *Permafrost and Periglacial Processes*, 2(4), 283–300.
674 <https://doi.org/10.1002/ppp.3430020404>
- 675 JCMS-IIIB5706, 2003. Monitoring method for active cracks in concrete by acoustic emission. Construction
676 Materials Standard, Federation of Construction Materials Industries, Japan, pp.23–28.

- 677 Jia, H., Xiang, W., & Krautblatter, M. (2015). Quantifying rock fatigue and decreasing compressive
678 and tensile strength after repeated freeze-thaw cycles. *Permafrost and Periglacial Processes*,
679 26(4), 368–377. <https://doi.org/10.1002/ppp.1857>
- 680 Mackay, J.R. (1974). Reticulate ice veins in permafrost, northern Canada. *Canadian Geotechnical*
681 *Journal*, 11(2), 230–237. <https://doi.org/10.1139/t74-019>
- 682 Matsuoka, N., & Murton, J. B. (2008). Frost weathering: recent advances and future directions.
683 *Permafrost and Periglacial Processes*, 19(2), 195–210. <https://doi.org/10.1002/ppp.620>
- 684 Maji V. (2018). *An experimental investigation of micro- and macrocracking mechanisms in rocks by*
685 *freeze–thaw cycling*. (Doctoral dissertation). Brighton: University of Sussex;
686 2018. <http://sro.sussex.ac.uk/79661/>
- 687 Maji, V., & Murton, J. B. (2020a). Experimental observations that active-layer deepening drives
688 deeper rock fracture. *Permafrost and Periglacial Processes*, 31(2), 296–310.
689 <https://doi.org/10.1002/ppp.2041>
- 690 Maji, V., & Murton, J. B. (2020b). Micro-computed tomography imaging and probabilistic modelling
691 of rock fracture by freeze–thaw. *Earth Surface Processes and Landforms*, 45(3), 666–680.
692 <https://doi.org/10.1002/esp.4764>
- 693 Michlmayr, G., Cohen, D., & Or, D. (2012). Sources and characteristics of acoustic emissions from
694 mechanically stressed geologic granular media—A review. *Earth-Science Reviews*, 112(3–4), 97–
695 114. <https://doi.org/10.1016/j.earscirev.2012.02.009>
- 696 Murton, J. B. (2018). Frost weathering of chalk. In Lawrence JA, Preene M, Lawrence UL, Buckley R.
697 (Eds.), *Engineering in Chalk: Proceedings of the Chalk 2018 Conference, 17–18 September 2018*,
698 *Imperial College, London*. (pp. 497–502). London: ICE Publishing.

- 699 Murton, J. B., Peterson, R., & Ozouf, J. C. (2006). Bedrock fracture by ice segregation in cold regions.
700 *Science*, 314(5802), 1127–1129. DOI: 10.1126/science.1132127
- 701 Murton, J. B., Coutard, J. P., Lautridou, J. P., Ozouf, J. C., Robinson, D. A., Williams, R. B. G.,
702 Guillemet, G., & Simmons, P. (2000). Experimental design for a pilot study on bedrock
703 weathering near the permafrost table. *Earth Surface Processes and Landforms*, 25(12):1281–
704 1294. [https://doi.org/10.1002/1096-9837\(200011\)25:12<1281::AID-ESP137>3.0.CO;2-U](https://doi.org/10.1002/1096-9837(200011)25:12<1281::AID-ESP137>3.0.CO;2-U)
- 705 Murton, J. B., Coutard, J. P., Ozouf, J. C., Lautridou, J.P., Robinson, D. A., & Williams, R. B. G. (2001).
706 Physical modelling of bedrock brecciation by ice segregation in permafrost. *Permafrost and*
707 *Periglacial Processes*, 12(3), 255–266. <https://doi.org/10.1002/ppp.390>
- 708 Murton, J. B., Ozouf, J. C., & Peterson, R. (2016). Heave, settlement and fracture of chalk during
709 temperature cycling above and below 0°C. *Geomorphology*, 270, 71–87.
710 <https://doi.org/10.1016/j.geomorph.2016.07.016>
- 711 Ohno, K., & Ohtsu, M. (2010). Crack classification in concrete based on acoustic emission.
712 *Construction and Building Materials*, 24, 2339–2346.
713 <https://doi:10.1016/j.conbuildmat.2010.05.004>
- 714 Rempel, A. W. (2011). Microscopic and environmental controls on the spacing and thickness of
715 segregated ice lenses. *Quaternary Research* 75(2), 316–324.
716 <https://doi.org/10.1016/j.yqres.2010.07.005>
- 717 Taber, S. (1930). The mechanics of frost heaving. *Journal of Geology*, 38(4), 303–317.
718 <https://www.jstor.org/stable/30058950>
- 719 Todak, H. N., Tsui, M., Ley, M. T., & Weiss, W. J. (2017). Evaluating freeze-thaw damage in concrete
720 with acoustic emissions and ultrasonics. In Shen, G. Wu, Z., and Zhang, J. (eds), *Advances in*
721 *Acoustic Emission Technology*. (Springer Proceedings in Physics 179, pp. 175–189). Switzerland:
722 Springer.

- 723 Walder, J. S., & Hallet, B. (1985). A theoretical model of the fracture of rock during freezing.
724 *Geological Society of America Bulletin*, 96(3), 336–346. <https://doi.org/10.1130/0016->
725 [7606\(1985\)96<336:ATMOTF>2.0.CO;2](https://doi.org/10.1130/0016-7606(1985)96<336:ATMOTF>2.0.CO;2)
- 726 Walder, J. S., & Hallet, B. (1986). The physical basis of frost weathering: Toward a more
727 fundamental and unified perspective. *Arctic and Alpine Research*, 18(1), 27–32. DOI:
728 [10.1080/00040851.1986.12004060](https://doi.org/10.1080/00040851.1986.12004060)
- 729 Wang, Y., Feng, W., Wang, H., Han, J., & Li, C. (2019). Geomechanical and acoustic properties of
730 intact granite subjected to freeze–thaw cycles during water-ice phase transformation in
731 Beizhan’s Open Pit Mine Slope, Xinjiang, China. *Water*, 11(11), 2309.
732 <https://doi.org/10.3390/w11112309>
- 733 Weber, S., Faillettaz, J., Meyer, M., Beutel, J., & Vieli, A. (2018). Acoustic and microseismic
734 characterization in steep bedrock permafrost on Matterhorn (CH). *Journal of Geophysical*
735 *Research: Earth Surface*, 123(6), 1363–1385. <https://doi.org/10.1029/2018JF004615>
736
737

738 Tables

739

740 **Table 1.** Number and magnitude of AE events occurred during freezing periods.

Cycles	Number of AE events	Amplitude (dB)					
		>40 & < 49	>49 & < 57	>57 & < 65	>65 & < 73	>73 & < 81	>81
F3	231	142	69	16	4	0	0
F4	751	506	176	55	14	0	0
F5	873	604	198	55	12	4	0
F10	43	23	9	10	1	0	0

741

742

743 **Table 2.** Number and magnitude of AE events occurred during freeze-to-thaw transitions.

Cycles	Number of AE events	Amplitude (dB)					
		>40 & < 49	>49 & < 57	>57 & < 65	>65 & < 73	73 & < 81	>81
FT1	1792	900	506	313	70	3	0
FT 2	448	159	148	98	33	10	0
FT 3	734	434	246	52	2	0	0
FT 4	195	129	47	18	1	0	0
FT 5	180	72	86	21	1	0	0
FT 6	533	335	121	62	14	1	0
FT 7	334	187	90	43	13	1	0
FT 8	119	88	23	4	4	0	0
FT 9	361	171	93	67	23	4	3
FT 10	252	110	79	38	22	3	0
FT 11	487	230	155	78	21	3	0
FT 12	476	280	140	44	11	1	0
FT 13	582	297	186	73	24	2	0
FT 14	520	386	108	23	3	0	0
FT 15	392	190	147	45	10	0	0
FT 16	11	7	4	0	0	0	0

744

745

746 **Table 3.** Number and magnitude of AE events occurred during thawing periods.

Cycles	Number of AE events	Amplitude (dB)					
		>40 & < 49	>49 & <57	>57 & < 65	>65 & < 73	>73 & < 81	>81
T1	4	2	1	1	0	0	0
T2	368	188	143	34	3	0	0
T3	647	393	206	48	0	0	0
T4	369	235	102	30	2	0	0
T5	395	211	157	26	1	0	0
T6	685	372	255	56	2	0	0
T7	4219	2488	1526	183	20	2	0
T8	730	46	252	432	0	0	0
T10	497	277	153	62	5	0	0
T11	585	307	206	60	12	0	0
T12	156	69	54	33	0	0	0
T13	294	148	124	22	0	0	0
T14	150	72	74	4	0	0	0
T16	5	5	0	0	0	0	0

747

748 **Table 4.** Number and magnitude of AE events during thaw-to-freeze transitions.

Cycles	Number of AE events	Amplitude (dB)					
		>40 & <49	>49 & < 57	>57 & < 65	>65 & <73	>73 & <81	>81
TF2	543	311	178	37	16	1	0
TF 3	255	177	66	12	0	0	0
TF 4	286	210	57	19	0	0	0
TF 5	222	144	65	12	1	0	0
TF 7	290	197	77	13	3	0	0
TF 8	11	0	0	11	0	0	0
TF 9	9	4	4	0	1	0	0
TF 13	8	3	4	1	0	0	0
TF 14	2	1	1	0	0	0	0
TF 15	14	12	1	1	0	0	0

749

750

751

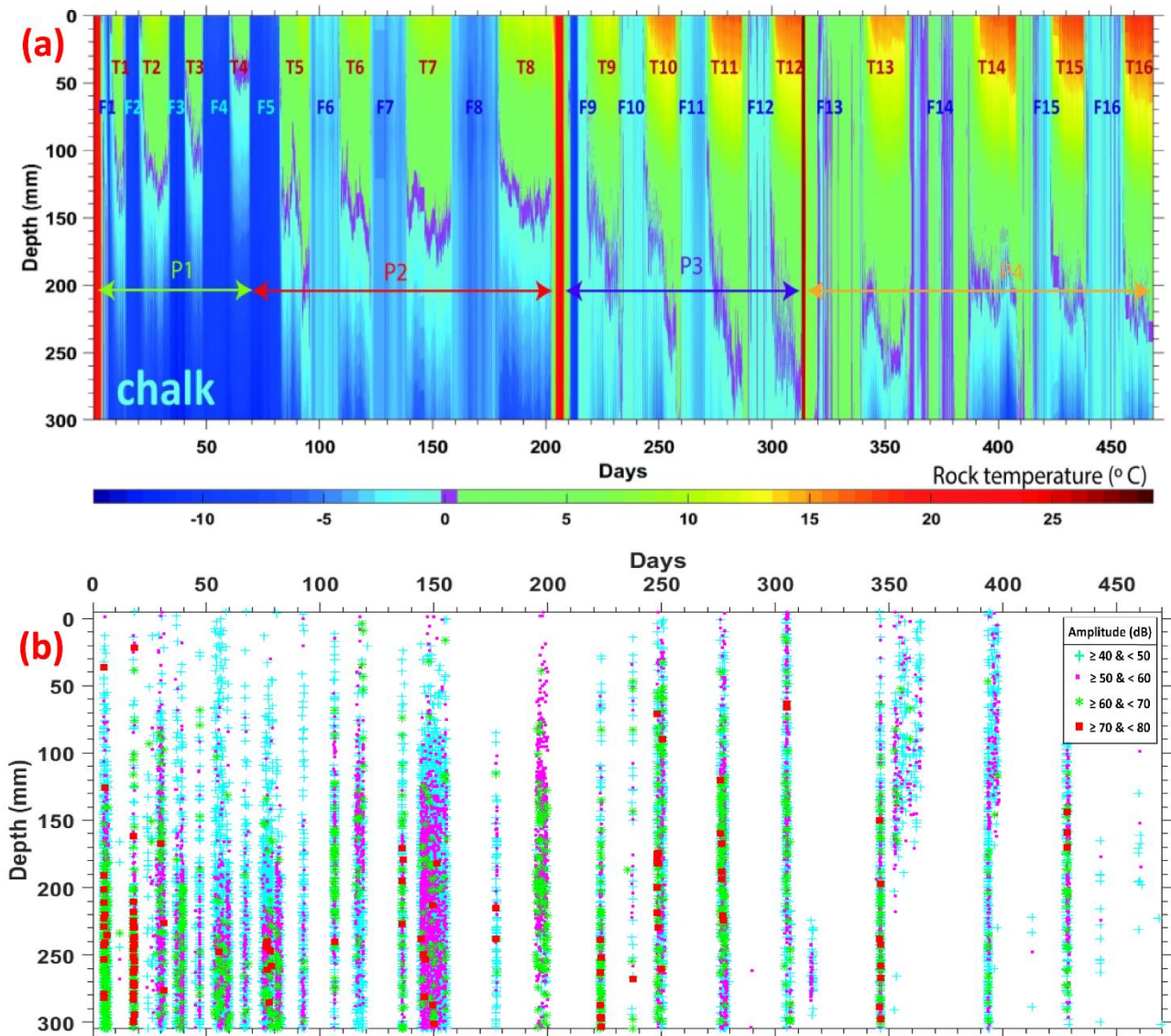
752 **Table 5.** Summary of probability (P) values based on Bayes' theorem for testing the hypothesis that
 753 inside-out (IO) mode of crack propagation is supported by tensional activity (T), whereas the
 754 outside-in (OI) mode is supported by shearing activity (S).

Part of freeze-thaw cycle	P(T IO)	P(IO T)	P(S OI)	P(OI S)
Freeze	0.57	0.68	0.73	0.67
Freeze-to-thaw	0.63	0.63	0.58	0.61
Thaw	0.73	0.66	0.54	0.69
Thaw-to-freeze	0.66	0.67	0.61	0.72

755

756

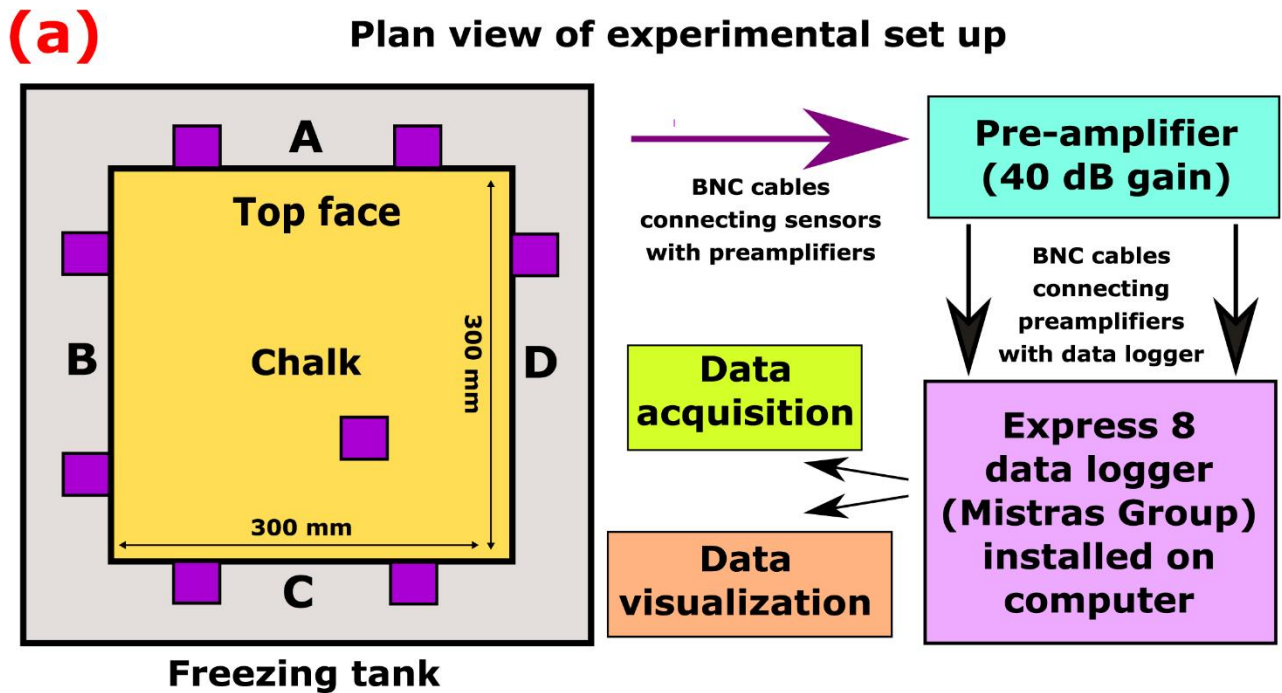
757 Figures
758



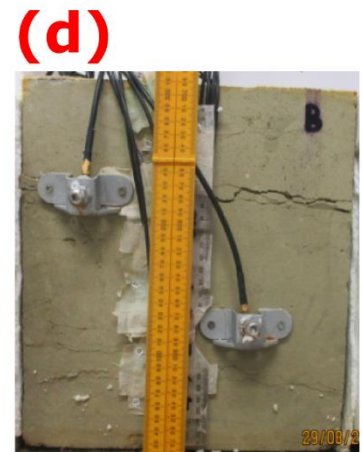
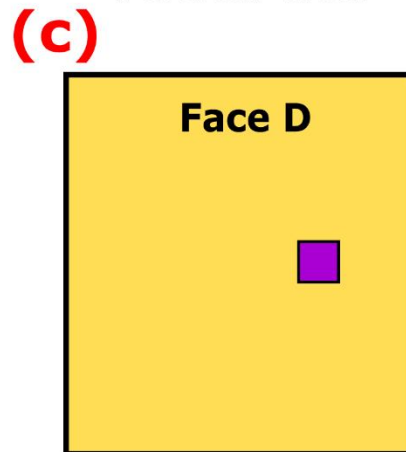
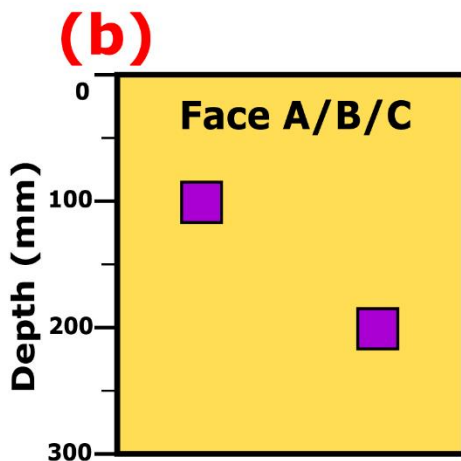
759

760 **Figure 1.** (a) Time series of vertical temperature profile (a) and amplitude of acoustic emission (AE)
761 events (b) in the chalk block during the 16 freeze–thaw cycles, divided into phases 1 to 4 (P1–P4).
762 F1 to F16 denote freezing periods, and T1 to T16 denote thawing periods.

763



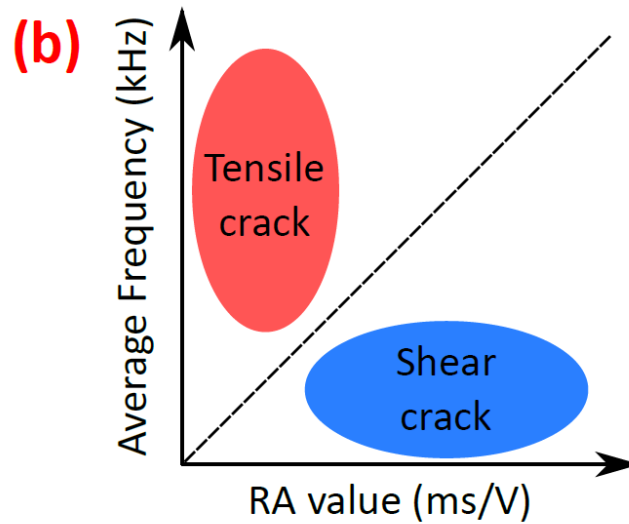
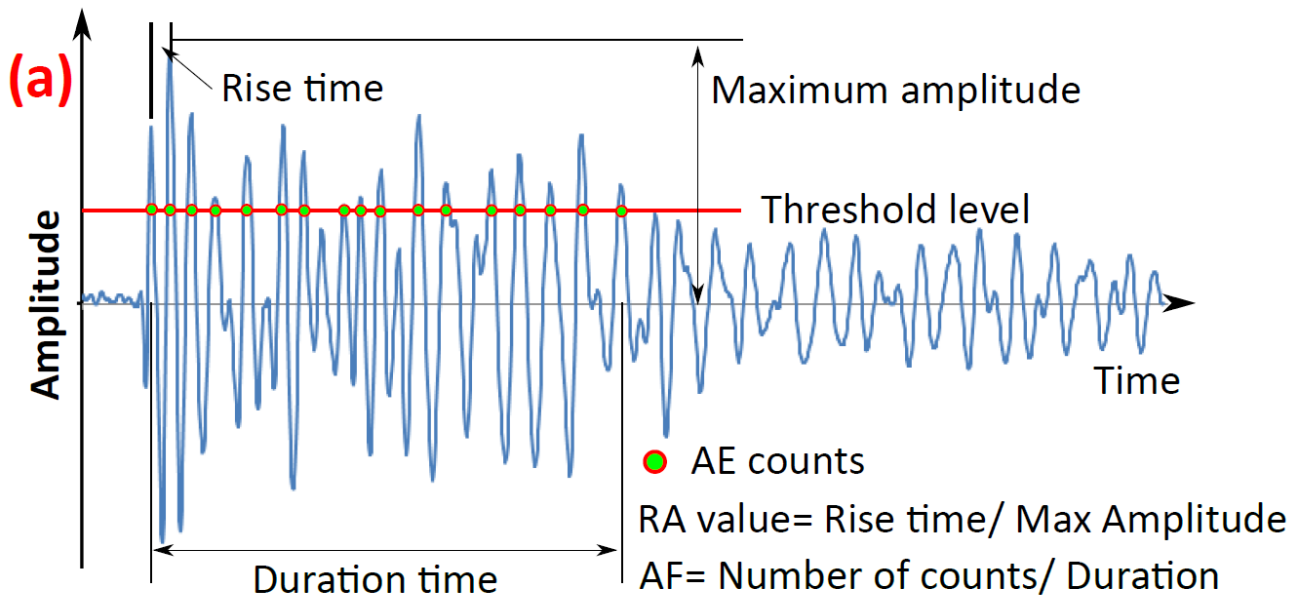
Vertical view



■ **Acoustic emission sensor**

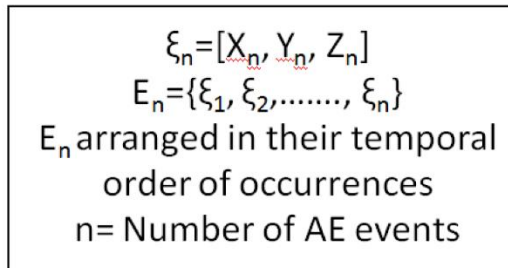
764
765 **Figure 2.** Diagrams showing locations of eight AE sensors on the chalk block. (a) Plan view of the top
766 face with layout of the experimental set up, illustrating the hardware interfaces. (b) Vertical view of
767 three faces A, B and C, each hosting two AE sensors along the diagonal. (c) Vertical view of face D,
768 with one AE sensor. (d) Photograph showing two AE sensors mounted on face B within metal cages
769 attached to the chalk block. Note well-developed brecciated horizon at ~100 mm depth and
770 incipient fractures at ~200 mm depth after 12 freeze–thaw cycles.

771

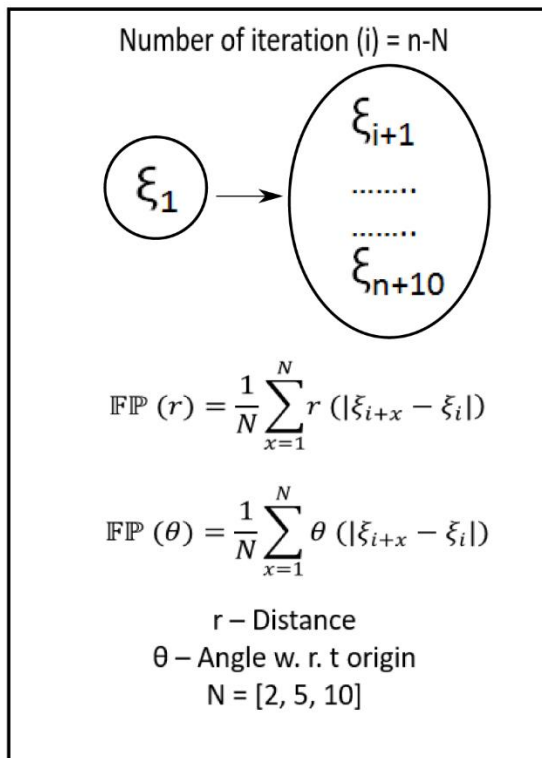


772
 773 **Figure 3.** Schematic diagrams of (a) different waveform parameters of the acoustic waves, (b) RA vs
 774 average frequency plot to discriminate tension and shear fracture. Source: modified from [Ohno et](#)
 775 [al., 2010.](#)
 776

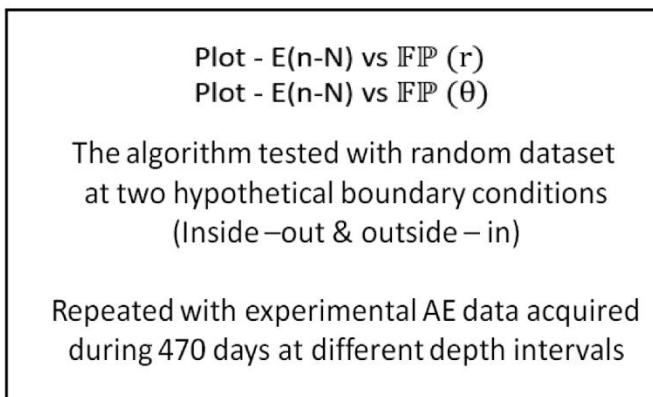
Input



Processing



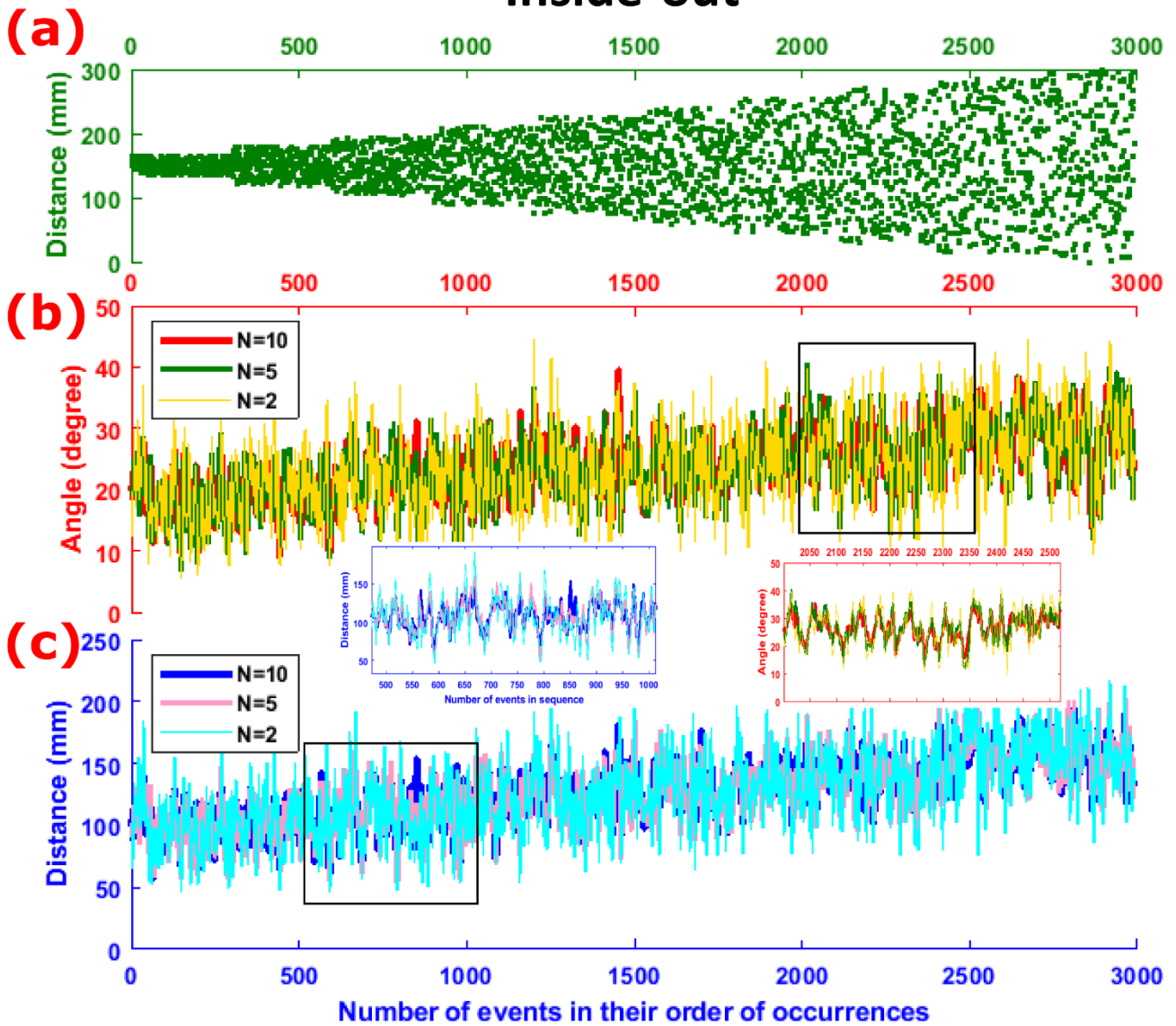
Output



777
778
779
780

Figure 4. Schematic diagram explaining the input of 3-D AE locations following their temporal occurrence, subsequent processing and final output of crack propagation hypothesis.

Inside-out



781

782

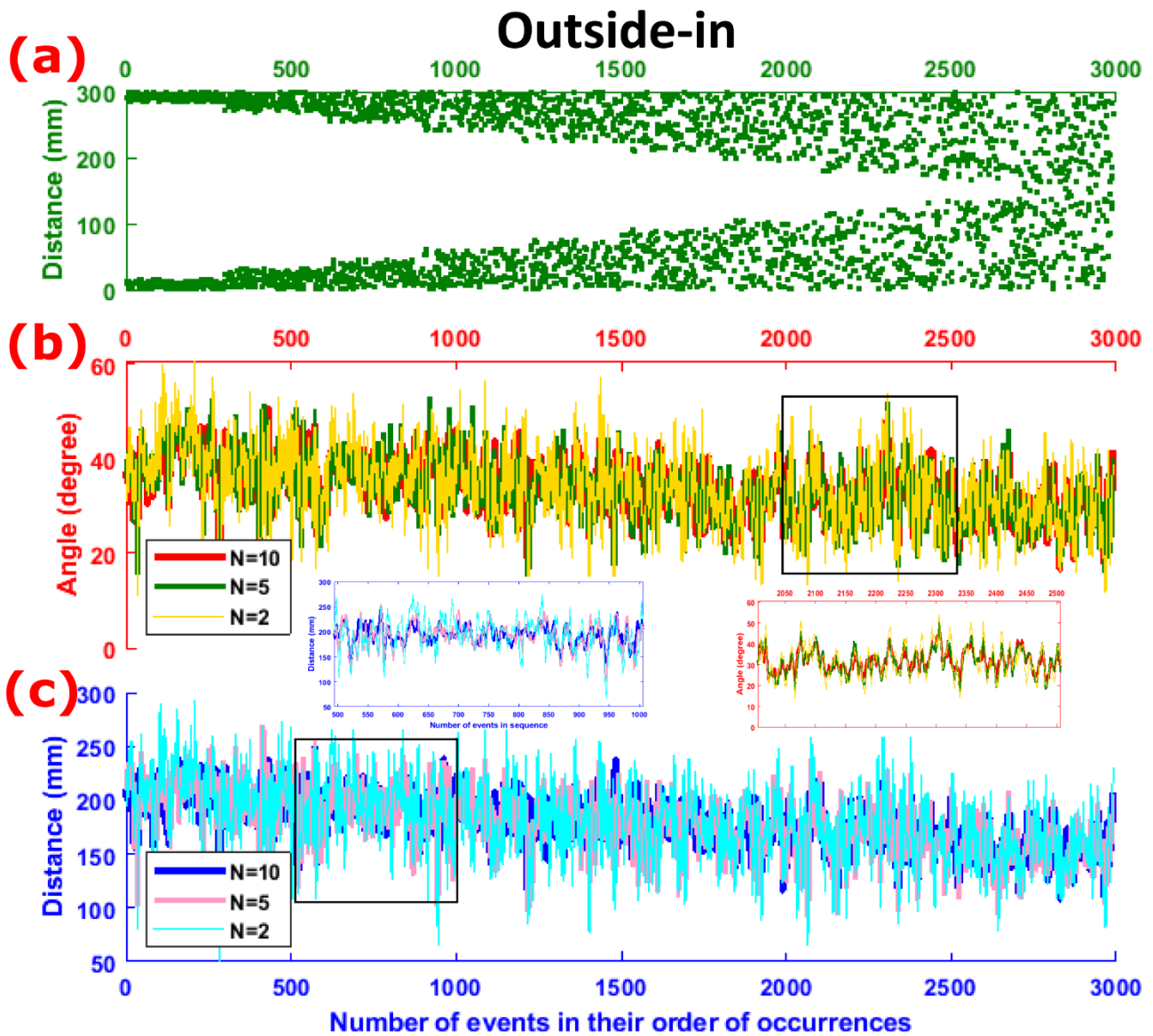
783

784

785

786

Figure 5. The inside-out model of fracture propagation. (a) Locations of the random points along Y-direction. (b) Angular relationships with varying number ($N=2, 5, 10$) of next consecutive events. (c) Distance relationships with $N=2, 5$ and 10 of next consecutive events. Inset figures show enlarged views of specific portions of the angular and distance variations marked by rectangular boxes.



787

788 **Figure 6.** The outside-in model of fracture propagation. (a) Locations of the random points along Y-

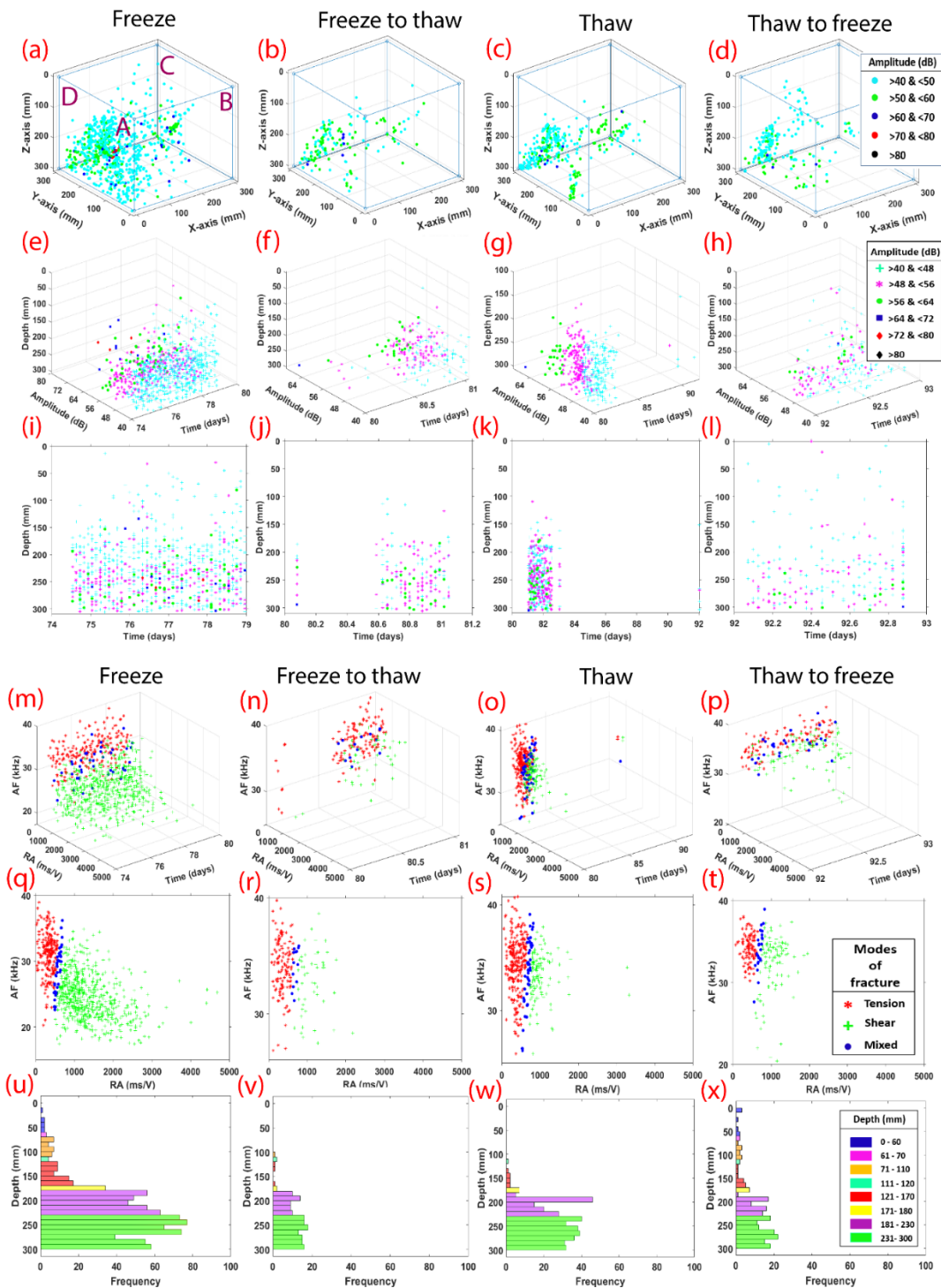
789 direction. (b) Angular relationships with varying number ($N=2, 5, 10$) of next consecutive events. (c)

790

791 Distance relationships with $N=2, 5, 10$ of next consecutive events. Inset figures show enlarged views

792

792 of specific portions of the angular and distance variations marked by rectangular boxes.



793

794

795

796

797

798

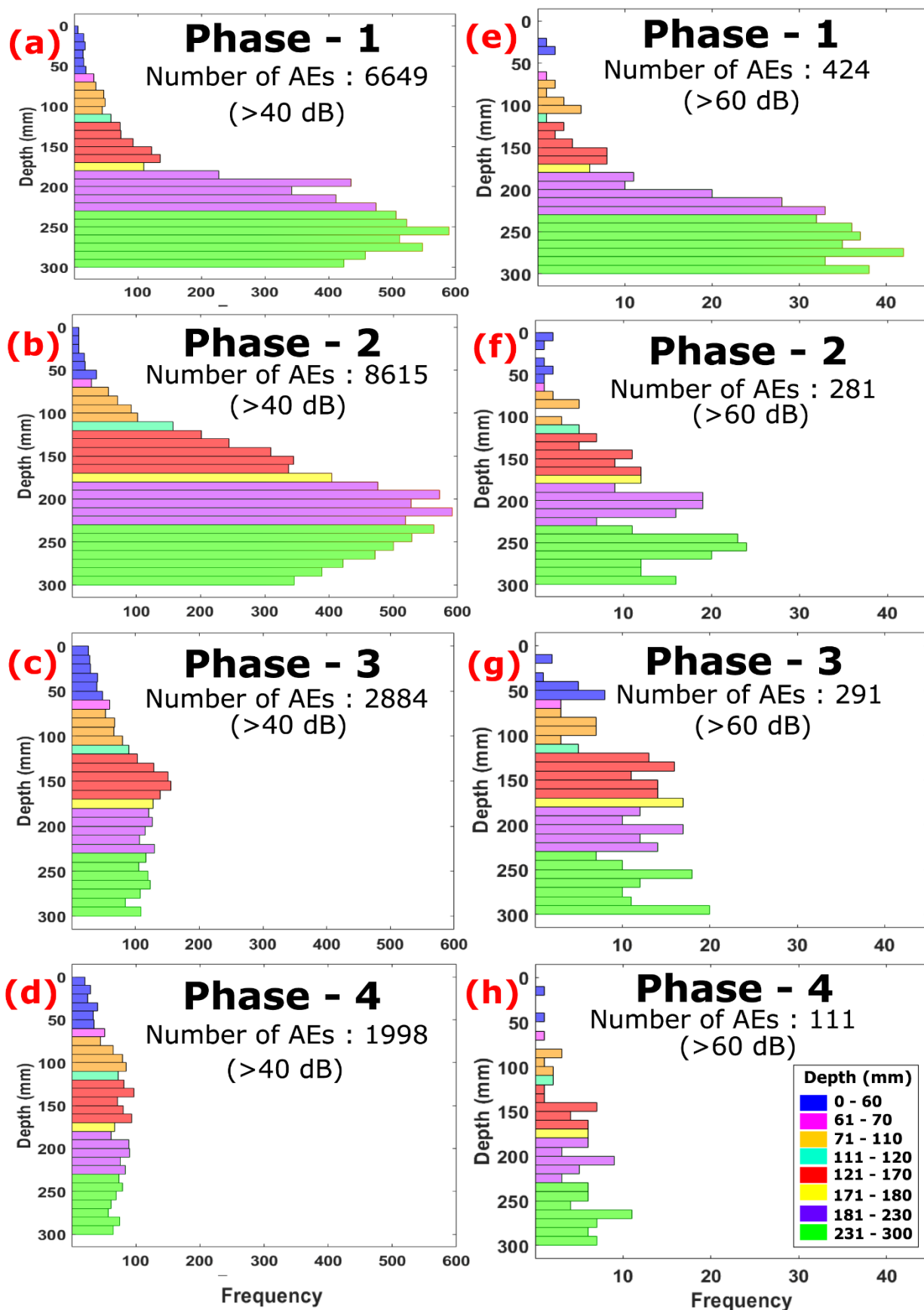
799

800

801

802

Figure 7. AE data for freeze–thaw cycle 5 divided into four constituent parts: freezing period ('freeze'), freeze-to-thaw transition, thawing period ('thaw') and thaw-to-freeze transition. (a–d) 3D locations of AE events with their respective amplitude. Vertical faces A–D of the block are labelled in (a); this labelling applies to all subsequent 3D plots in the article. (e–h) Visualization of AE events in terms of depth, amplitude and time. (i–l) Simplified version of plots e–h with depth vs time, and amplitude ranges marked with different shapes and colours. (m–p) Visualization of AE events in terms of AF values, RA values and time, labelled according to modes of fracture. (q–t) Simplified version of plots m–p with AF vs RA values and fracture modes. (u–x) Frequency distribution of AE events along various depth intervals within the block.

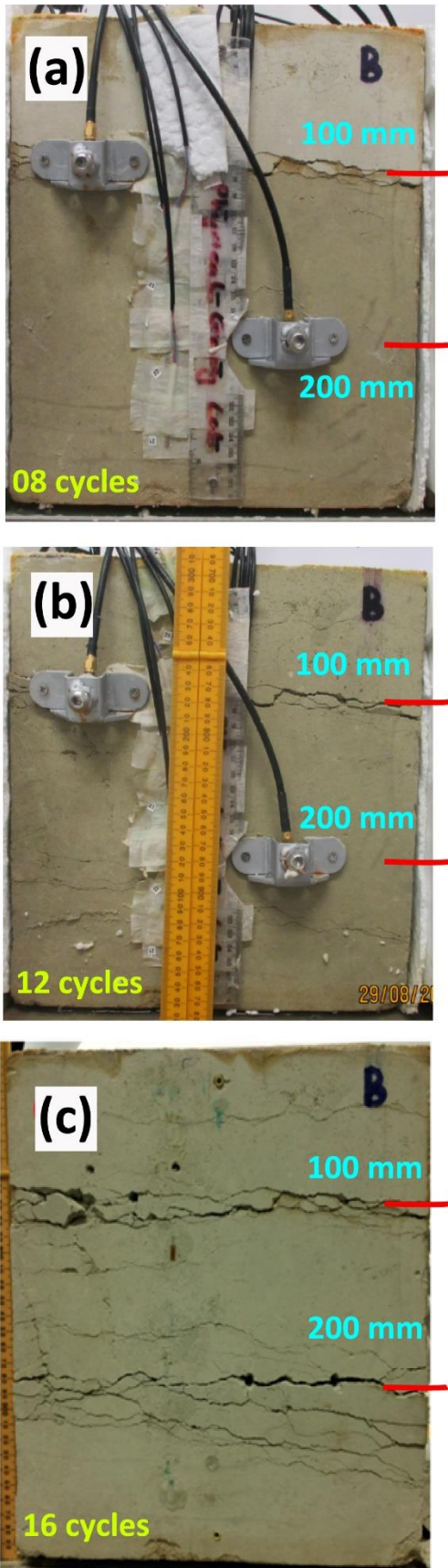


803

804

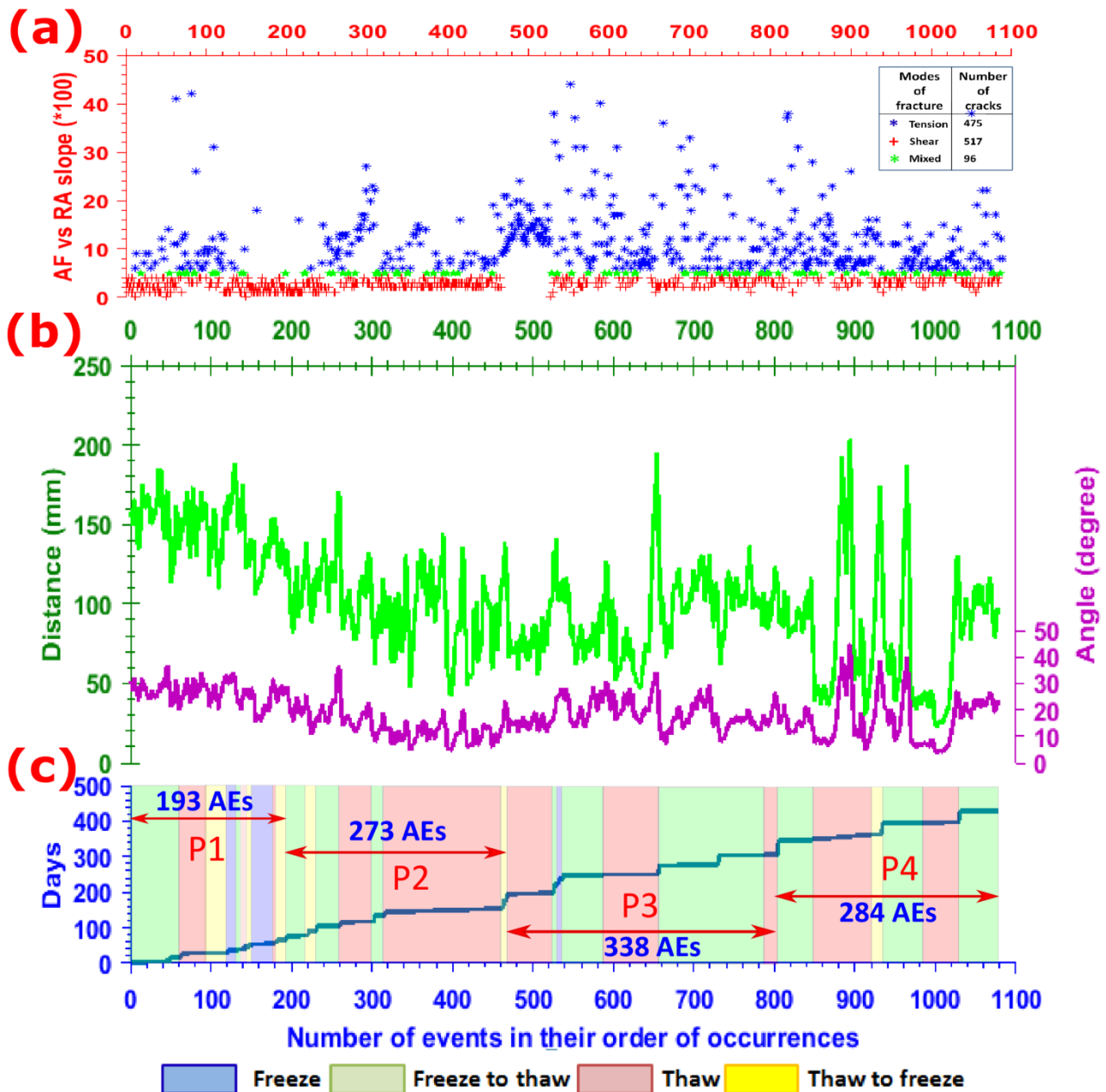
805

Figure 8. Acoustic emission (AE) frequency versus depth during phases 1 to 4 of the experiment. (a–d) All AEs (>40dB), (e–h) AEs of higher magnitude (>60 dB).



806
 807 **Figure 9.** Photographs of macrocracks and brecciated horizons in vertical face B of the chalk block
 808 after 8, 12 and 16 freeze–thaw cycles (a–c, respectively). Depth intervals used for the analysis of
 809 the crack propagation models are marked.

70 - 110 mm depth (Upper brecciated horizon)



810

811 **Figure 10.** AE events within the 70–120 mm depth interval arranged in their order of occurrence

812 during the four phases (P1–4) of the experiment. (a) AE events classified as tension, shear and

813 mixed modes of cracking based on the parametric analysis of AE waveforms, using AF vs RA values.

814 (b) FIP (r) and FIP (θ) values indicated on Y-axes on left and right, respectively, of the corresponding

815 events. (c) Timing of AE events during P1–4 and subdivided into the four constituent parts of the

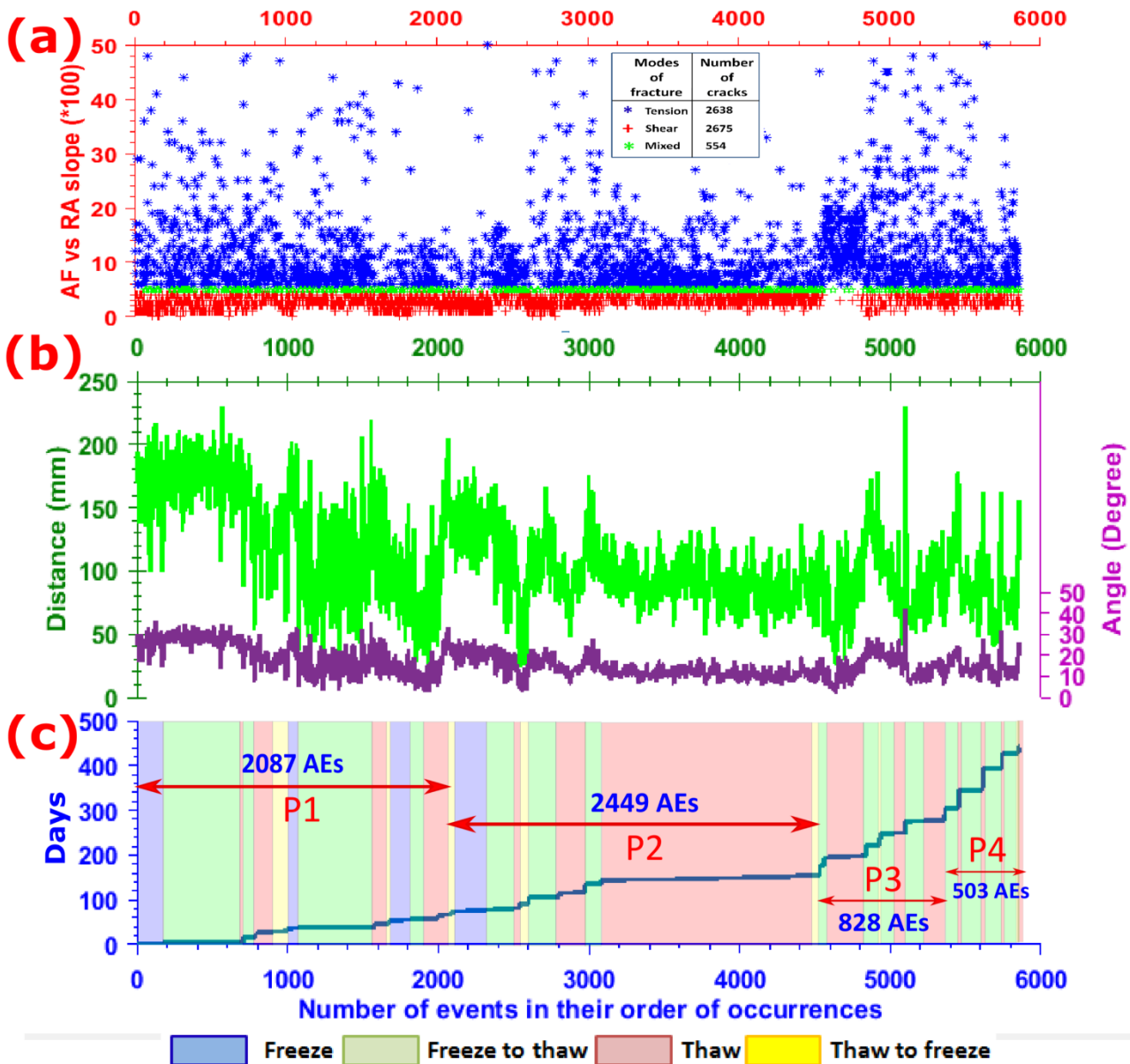
816 freeze–thaw cycles (freeze, freeze-to-thaw transition, thaw, and thaw-to-freeze transitions).

817

818

819

180 - 220 mm depth (Lower brecciated horizon)



820

821

822

823

824

825

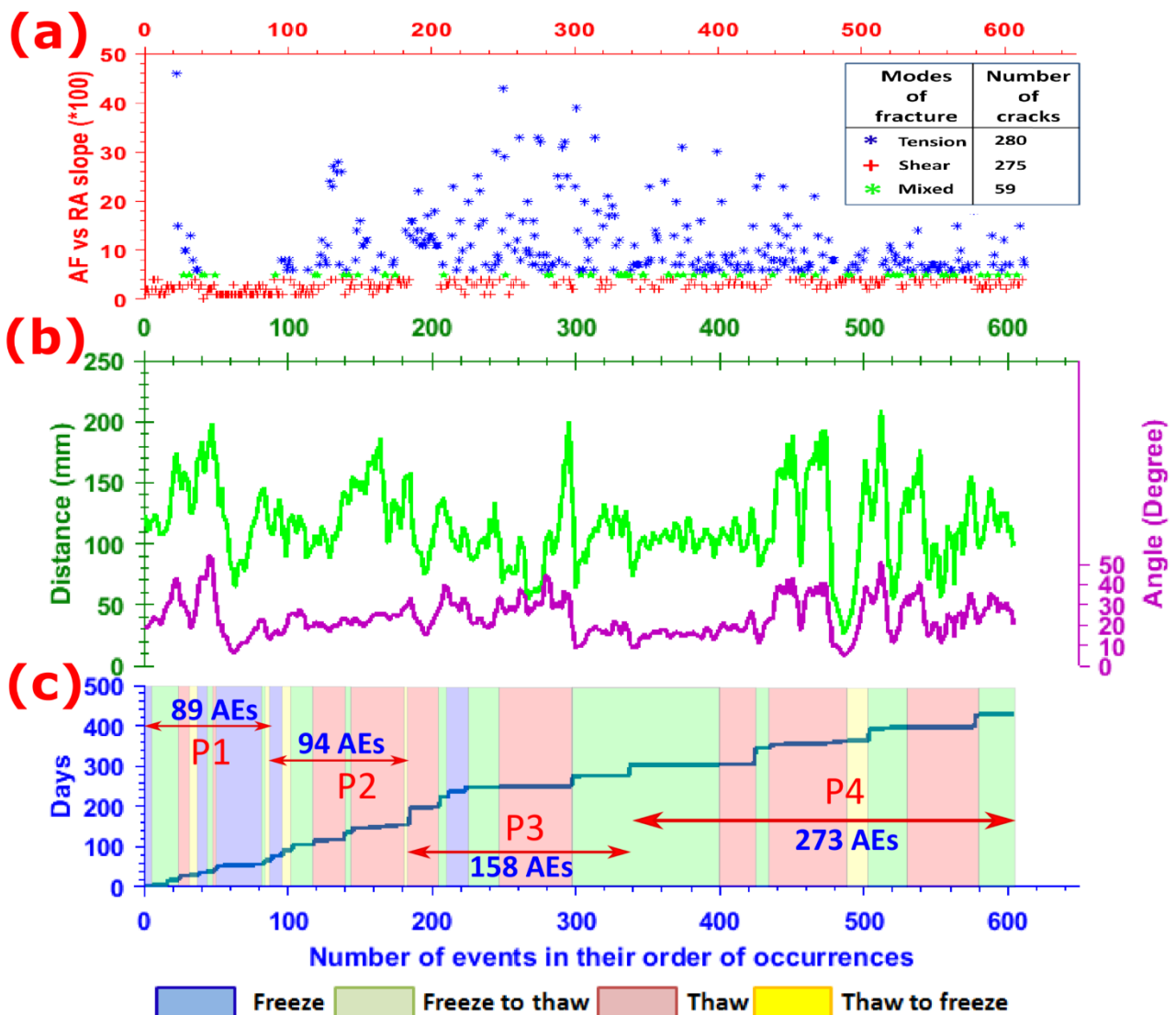
826

827

828

Figure 11. AE events within the 180–220 mm depth interval arranged in their order of occurrence during the four phases (P1–4) of the experiment. (a) AE events classified as tension, shear and mixed modes of cracking based on the parametric analysis of AE waveforms, using AF vs RA values. (b) FIP (r) and FIP (θ) values indicated on Y-axes on left and right, respectively, of the corresponding events. (c) Timing of AE events during P1–4 and subdivided into the four constituent parts of the freeze–thaw cycles (freeze, freeze-to-thaw transition, thaw, and thaw-to-freeze transitions).

**00 - 60 mm depth
(Upper horizon of limited fracture)**



829

830

831

832

833

834

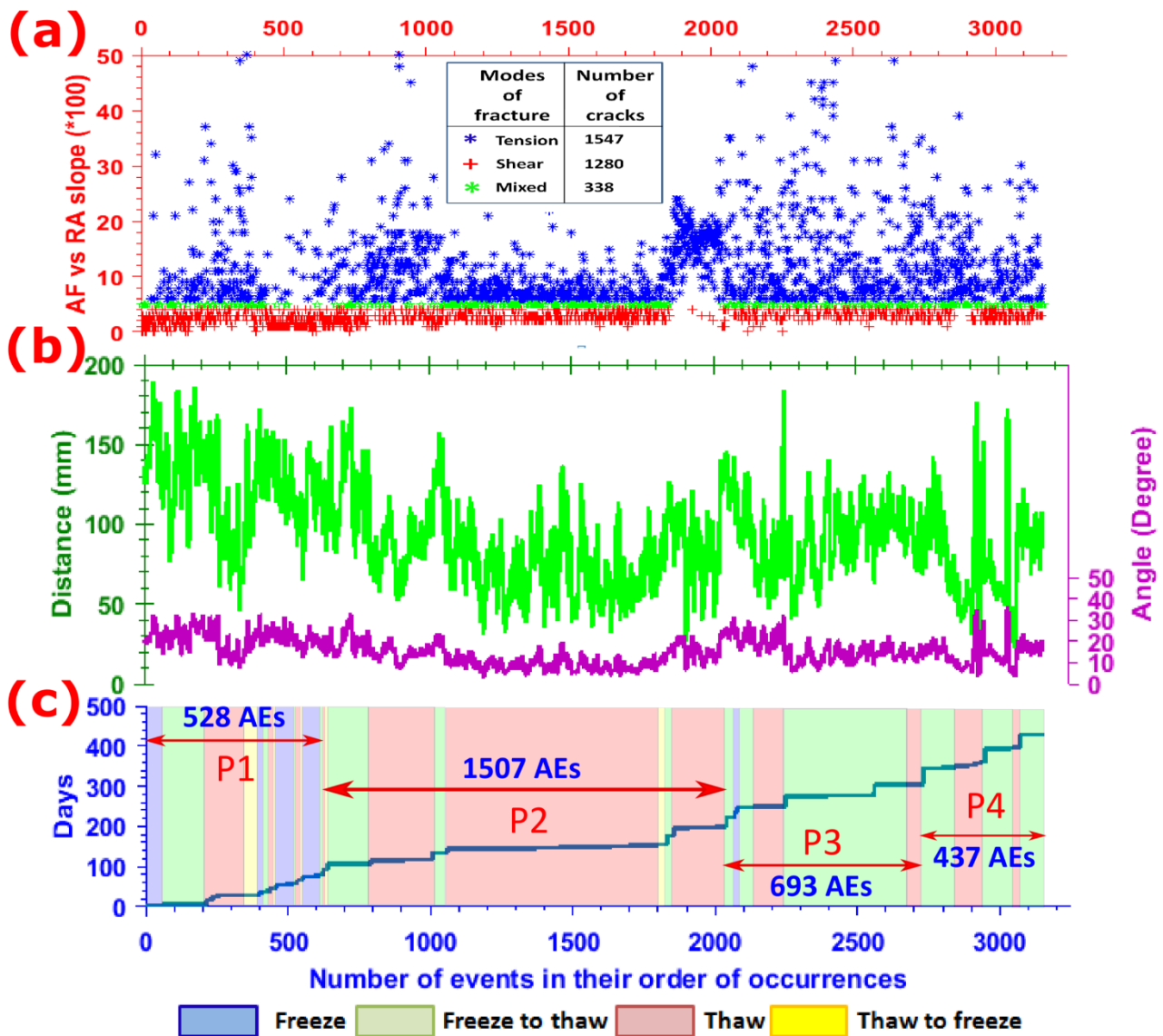
835

836

837

Figure 12. AE events within the 0–60 mm depth interval arranged in their order of occurrence during the four phases (P1–4) of the experiment. (a) AE events classified as tension, shear and mixed modes of cracking based on the parametric analysis of AE waveforms, using AF vs RA values. (b) FFP (r) and FFP (θ) values indicated on Y-axes on left and right, respectively, of the corresponding events. (c) Timing of AE events during P1–4 and subdivided into the four constituent parts of the freeze–thaw cycles (freeze, freeze-to-thaw transition, thaw, and thaw-to-freeze transitions).

120 - 170 mm depth (Lower horizon of limited fracture)



838

839

840

841

842

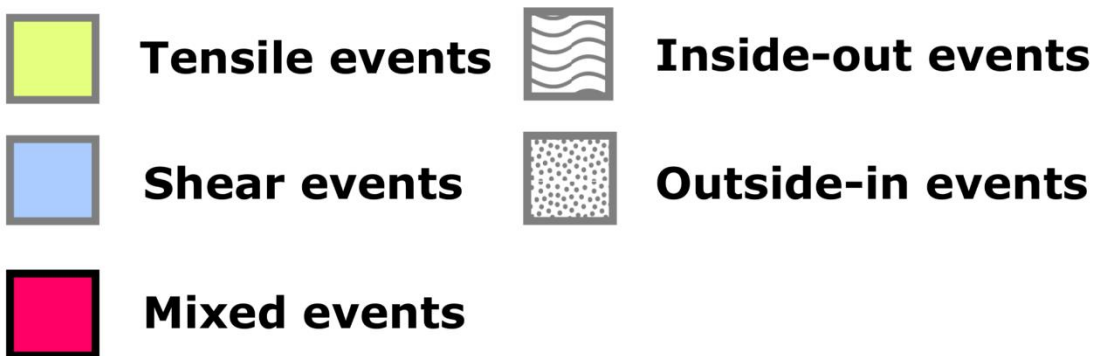
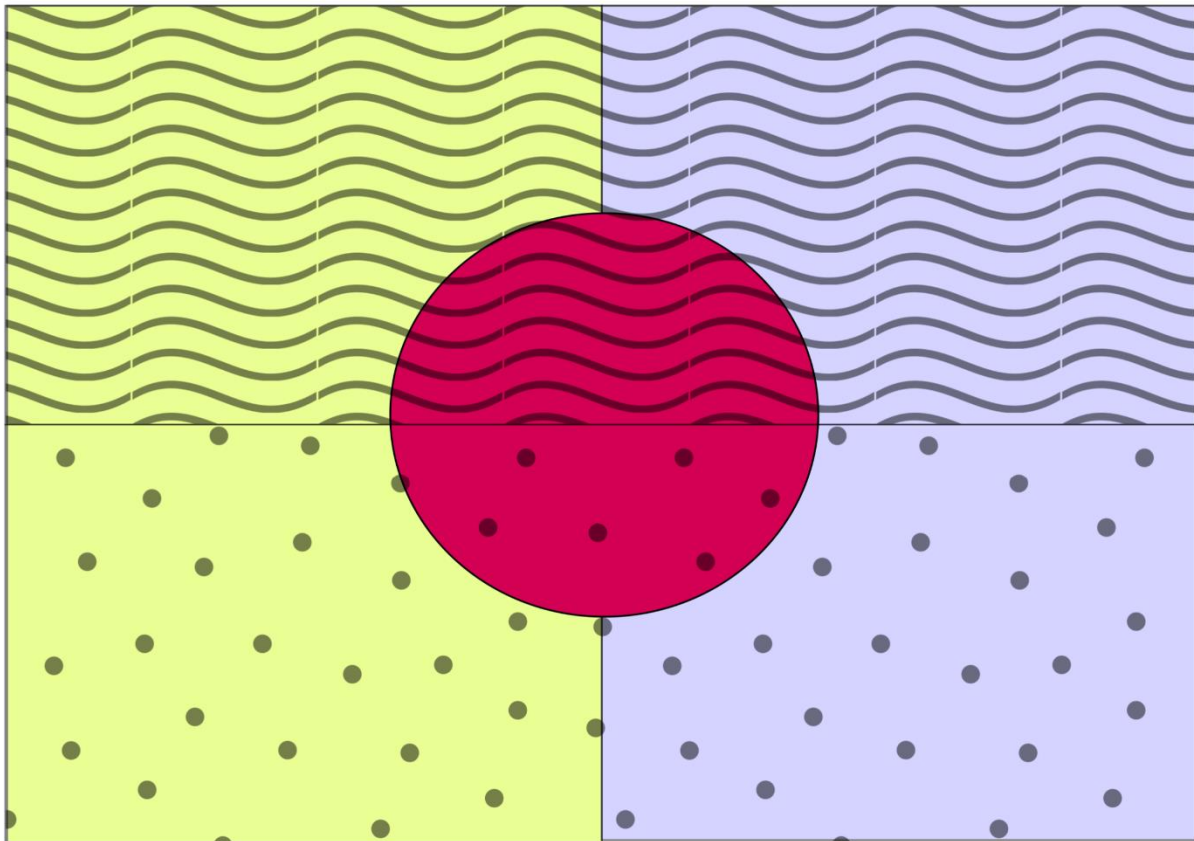
843

844

845

846

Figure 13. AE events within the 120–170 mm depth interval arranged in their order of occurrence during the four phases (P1–4) of the experiment. (a) AE events classified as tension, shear and mixed modes of cracking based on the parametric analysis of AE waveforms, using AF vs RA values. (b) FIP (r) and FIP (θ) values indicated on Y-axes on left and right, respectively, of the corresponding events. (c) Timing of AE events during P1–4 and subdivided into the four constituent parts of the freeze–thaw cycles (freeze, freeze-to-thaw transition, thaw, and thaw-to-freeze transitions).



847

848

849

850

851

Figure 14. Venn diagram illustration of various conventional modes of cracking (tension, shear and mixed) along with the proposed boundary situations of crack coalescence mechanisms (inside-out and outside-in).

852

Supporting Information

853

Figures S1–S20.

854

Experimental observations and statistical modelling of crack propagation dynamics in limestone by acoustic emission analysis during freezing and thawing

Vikram Maji^{1,2} and Julian B. Murton¹

1. Permafrost Laboratory, Department of Geography, University of Sussex, Brighton, BN1 9QJ, UK

2. Current address: Experimental Rock Deformation Laboratory, Department of Earth Sciences, IIT Kanpur, Uttar Pradesh- 208016, India

Contents of this file

Figures S1 to S20

Introduction

The supporting information provides 20 figures showing the full dataset for the acoustic emission (AE) results from the 16 cycles of freeze-thaw during a laboratory experiment lasting 470 days (Figures S1–S20). Each cycle has four parts: (1) a thaw-to-freeze transition, (2) a freezing period, (3) a freeze-to-thaw transition, and (4) a thawing period, as described in section 2.1 of the main paper. The data were collected by eight AE sensors installed on a 300-mm cubic block of chalk. An AE event was identified if at least four of the eight sensors captured the pulses of energy released (hits). Only AE events whose magnitude exceeds 40dB are shown, to exclude noise in the laboratory from signals of microcracking events. The three-dimensional location, depth magnitude, AF and RA values of >40dB AE events are shown in Figures S1–S20.

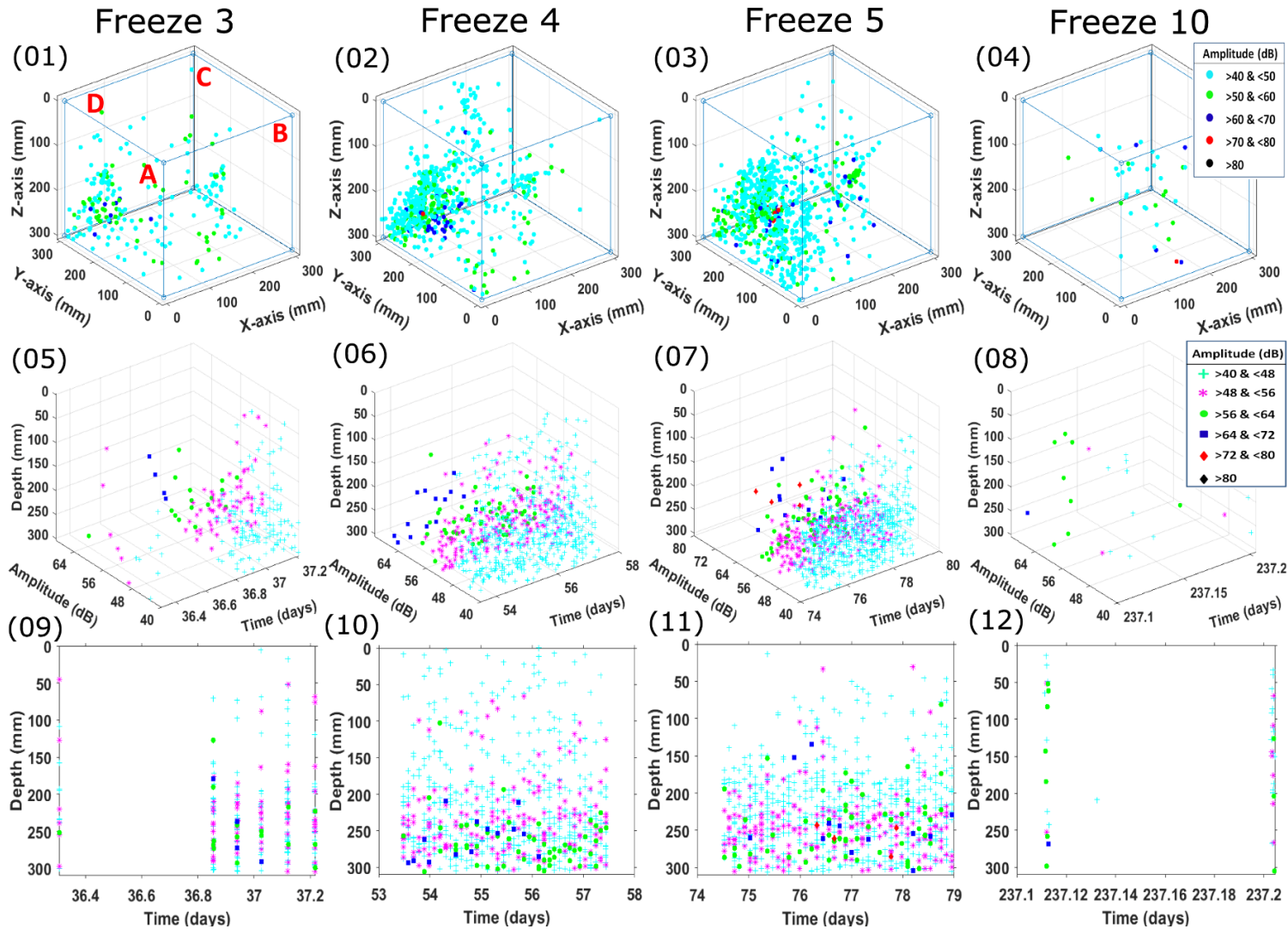


Figure S1. AE data for freezing periods. (01–04) 3D locations of AE events with their respective amplitude. Vertical faces A–D of the block are labelled in (01). (05–08) Visualization of AE events in terms of depth, amplitude and time. (09–12) Simplified version of plots 05–08 with depth vs time, and amplitude ranges marked with different shapes and colours.

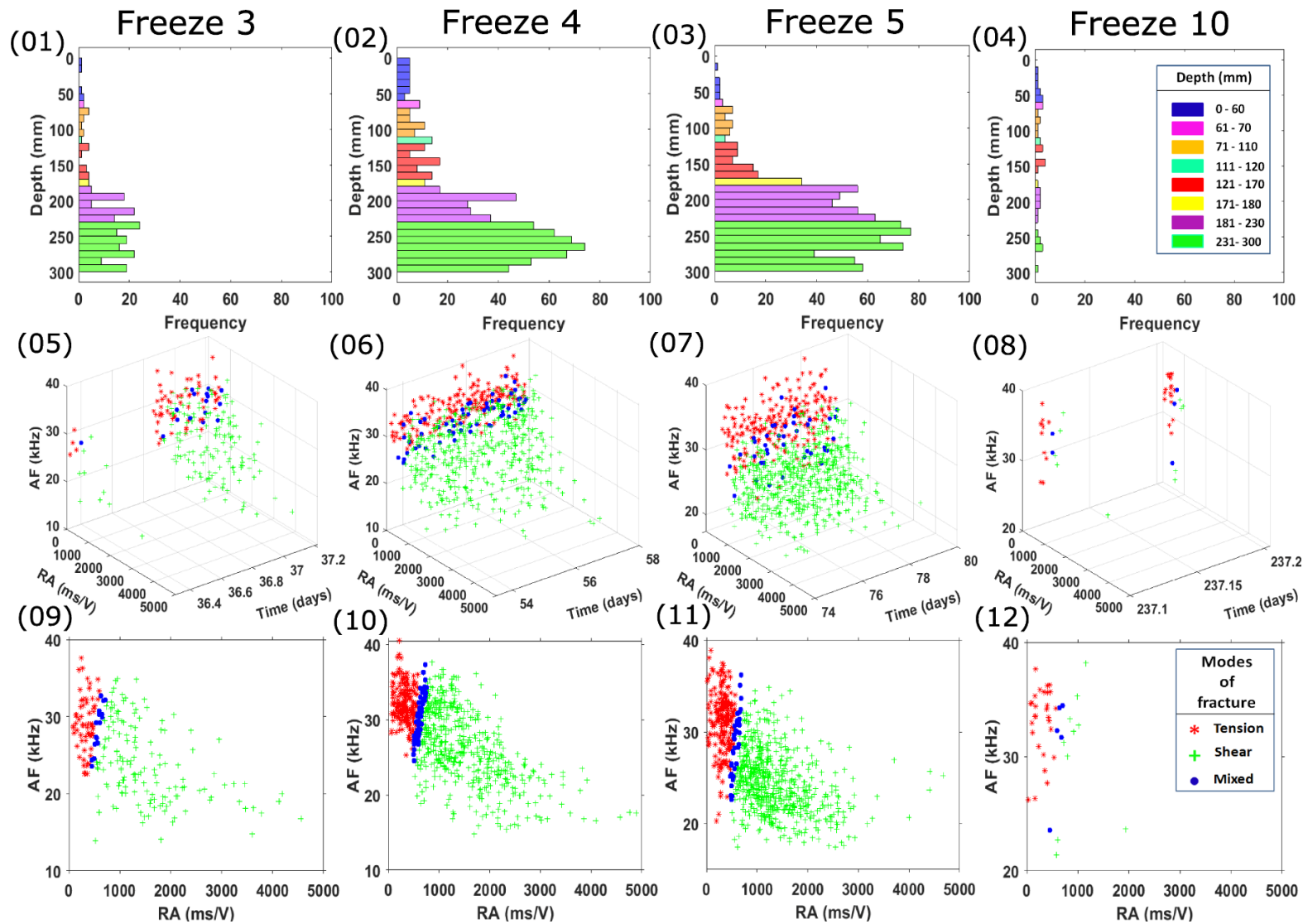


Figure S2. AE data for freezing periods. (01–04) Frequency distribution of AE events along various depth intervals within the block. (05–08) Visualization of AE events in terms of AF values, RA values and time, labelled according to modes of fracture. (09–12) Simplified version of plots 05–08 with AF vs RA values and fracture modes.

Freeze to thaw transition

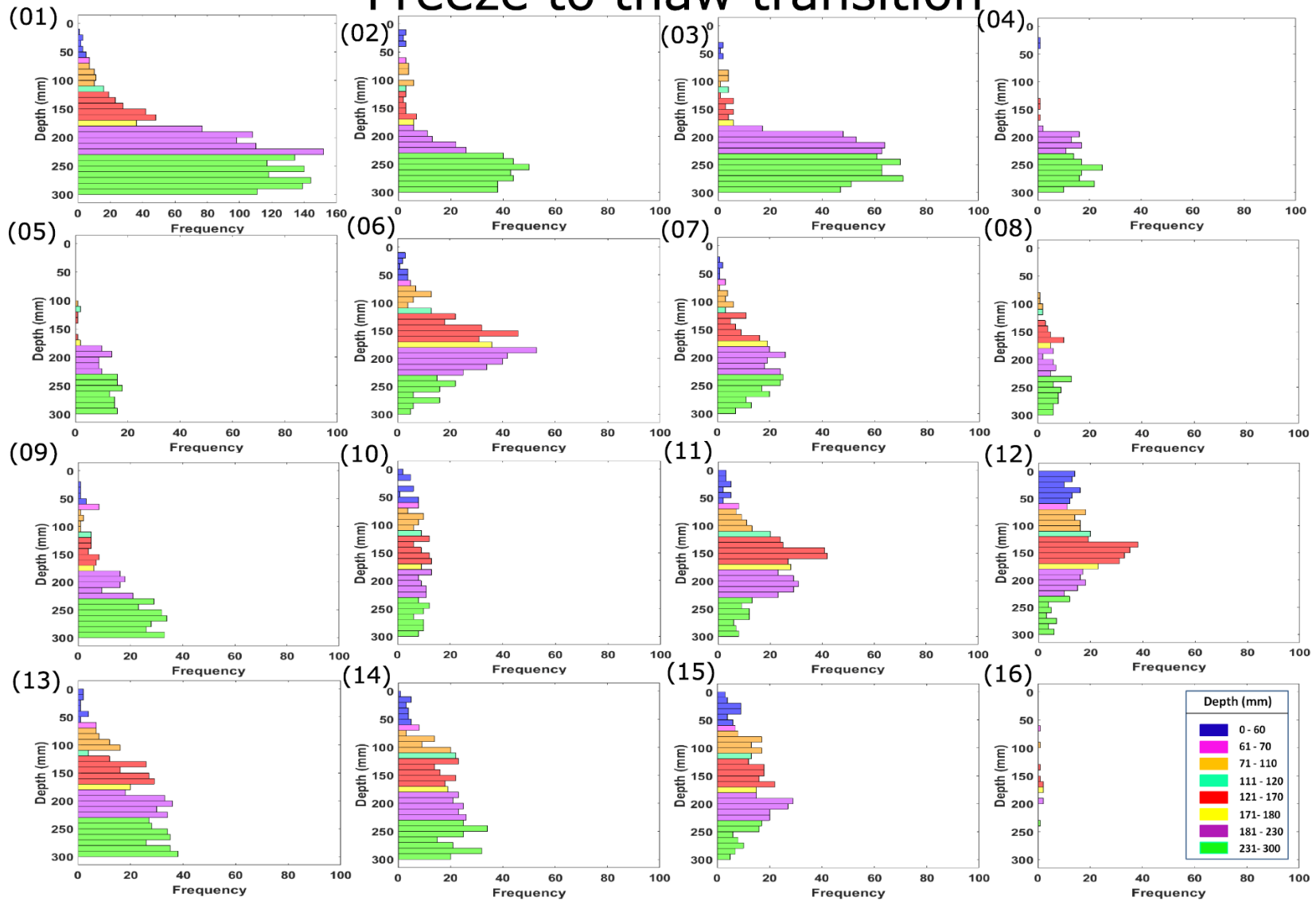


Figure S3. Frequency distribution of AE events along various depth intervals within the block recorded during freeze-to-thaw transitions over the course of 16 freeze-thaw cycles. The number beside each subpanel indicates the number of the respective cycle.

Freeze to thaw transition

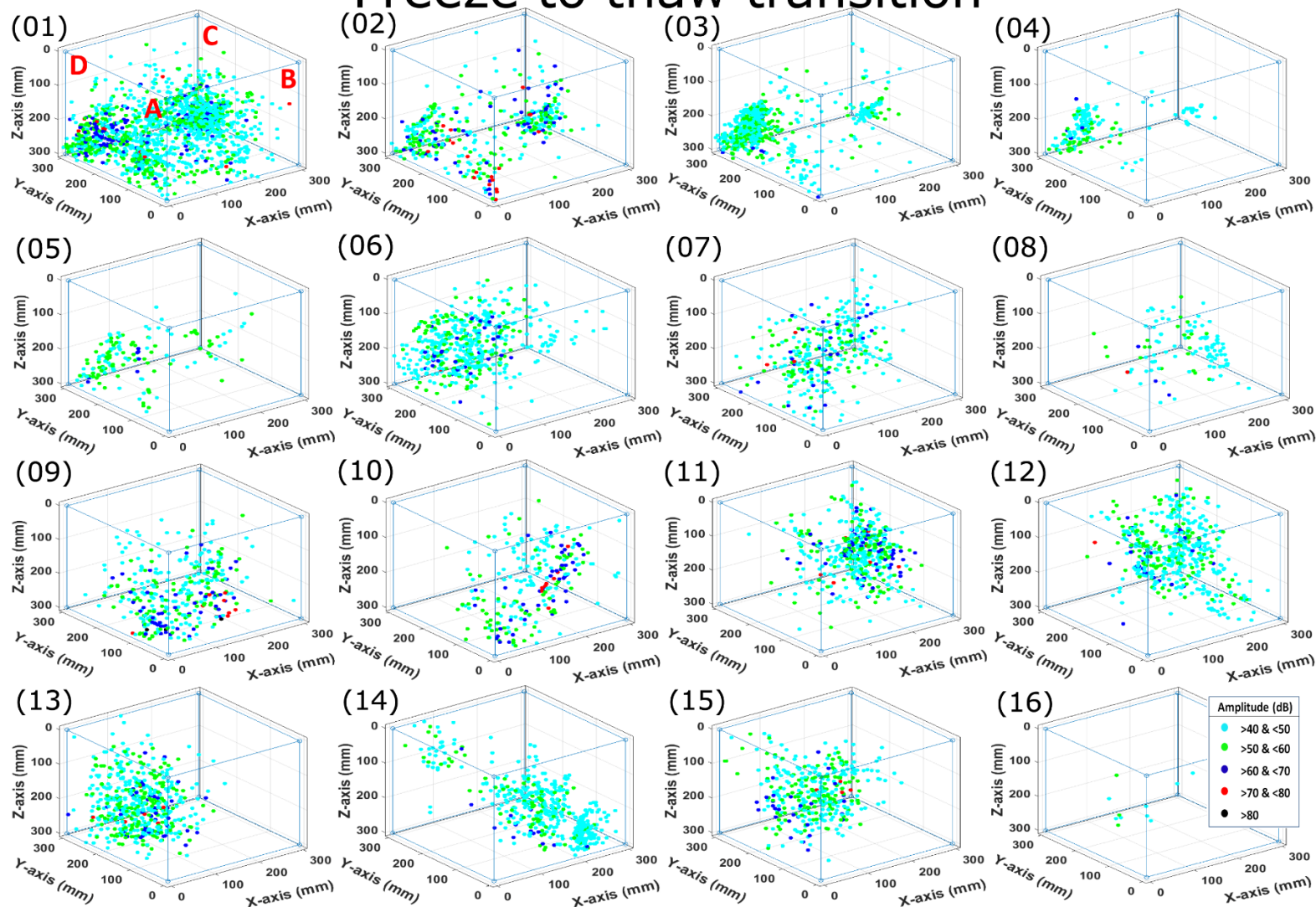


Figure S4. 3D locations of AE events with their respective amplitude recorded during freeze-to-thaw transitions over the course of 16 freeze-thaw cycles. Vertical faces A–D of the block are labelled in (01). The number beside each subpanel indicates the number of the respective cycle.

Freeze to thaw transition

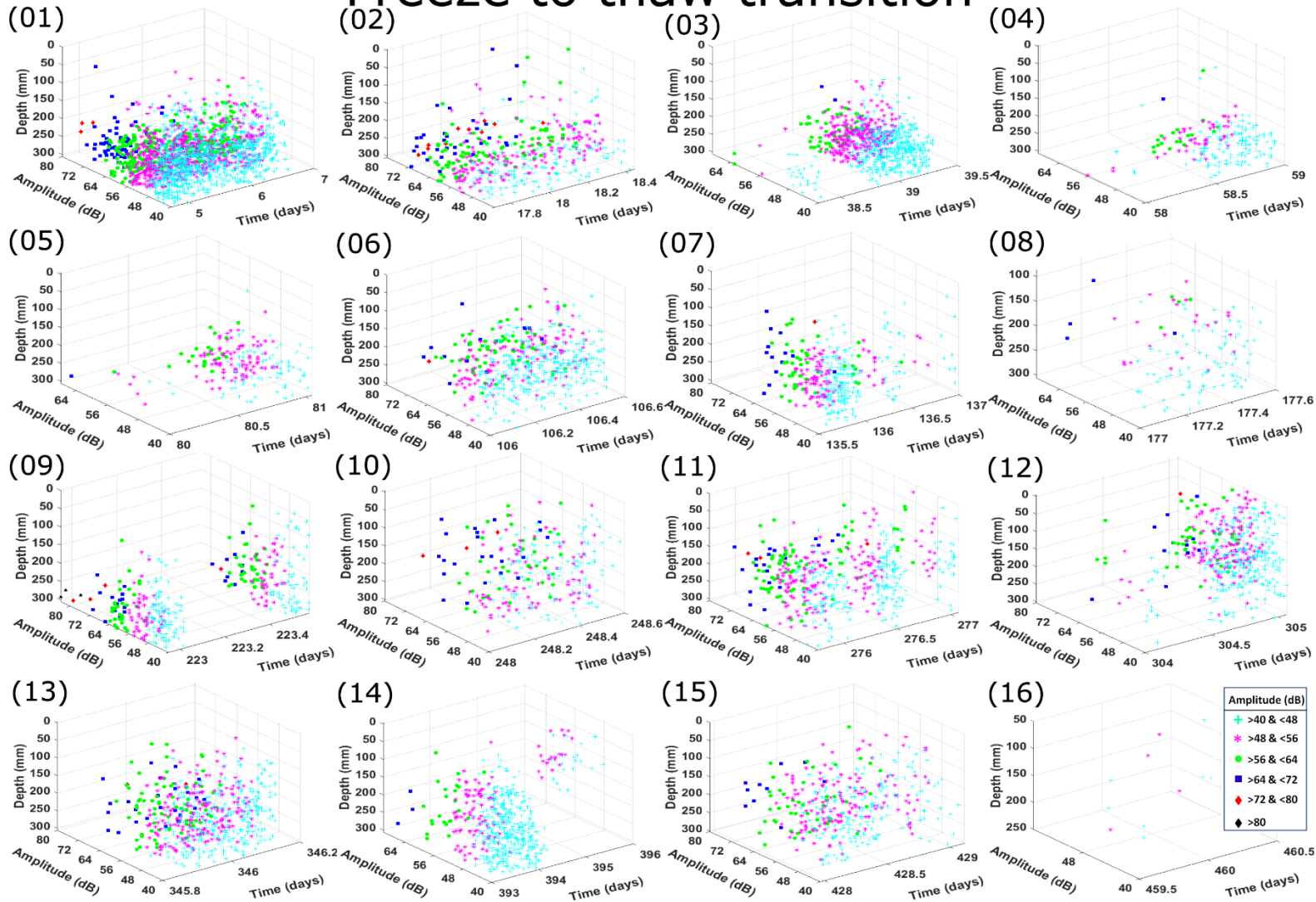


Figure S5. Visualization of AE events in terms of depth, amplitude and time recorded during freeze-to-thaw transitions over the course of 16 freeze-thaw cycles. The number beside each subpanel indicates the number of the respective cycle.

Freeze to thaw transition

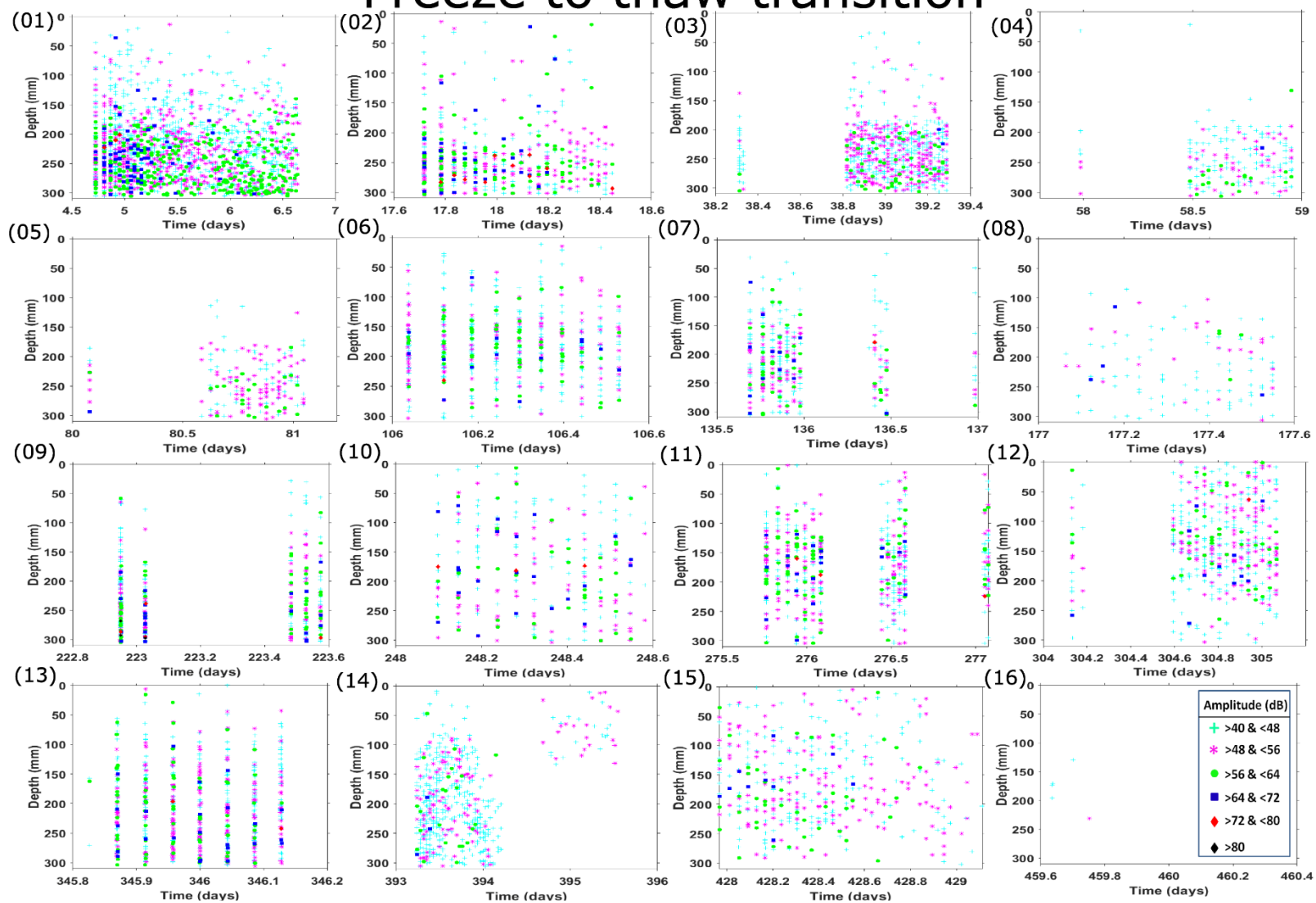


Figure S6. Simplified version of **Figure S5** with depth vs time, and amplitude ranges marked with different shapes and colours. The number beside each subpanel indicates the number of the respective cycle.

Freeze to thaw transition

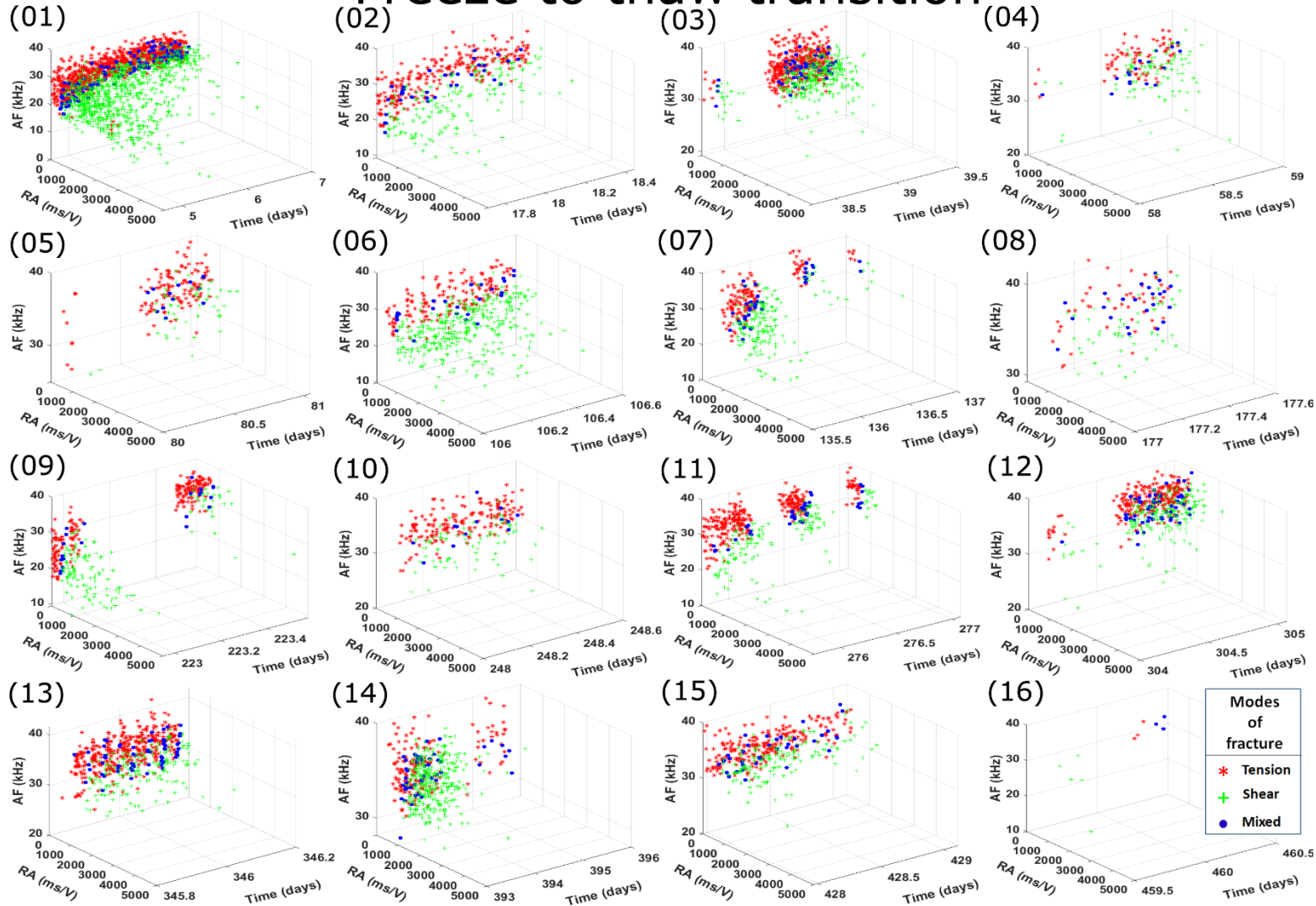


Figure S7. Visualization of AE events in terms of AF values, RA values and time, labelled according to modes of fracture and recorded during freeze-to-thaw transitions over the course of 16 freeze-thaw cycles. The number beside each subpanel indicates the number of the respective cycle.

Freeze to thaw transition

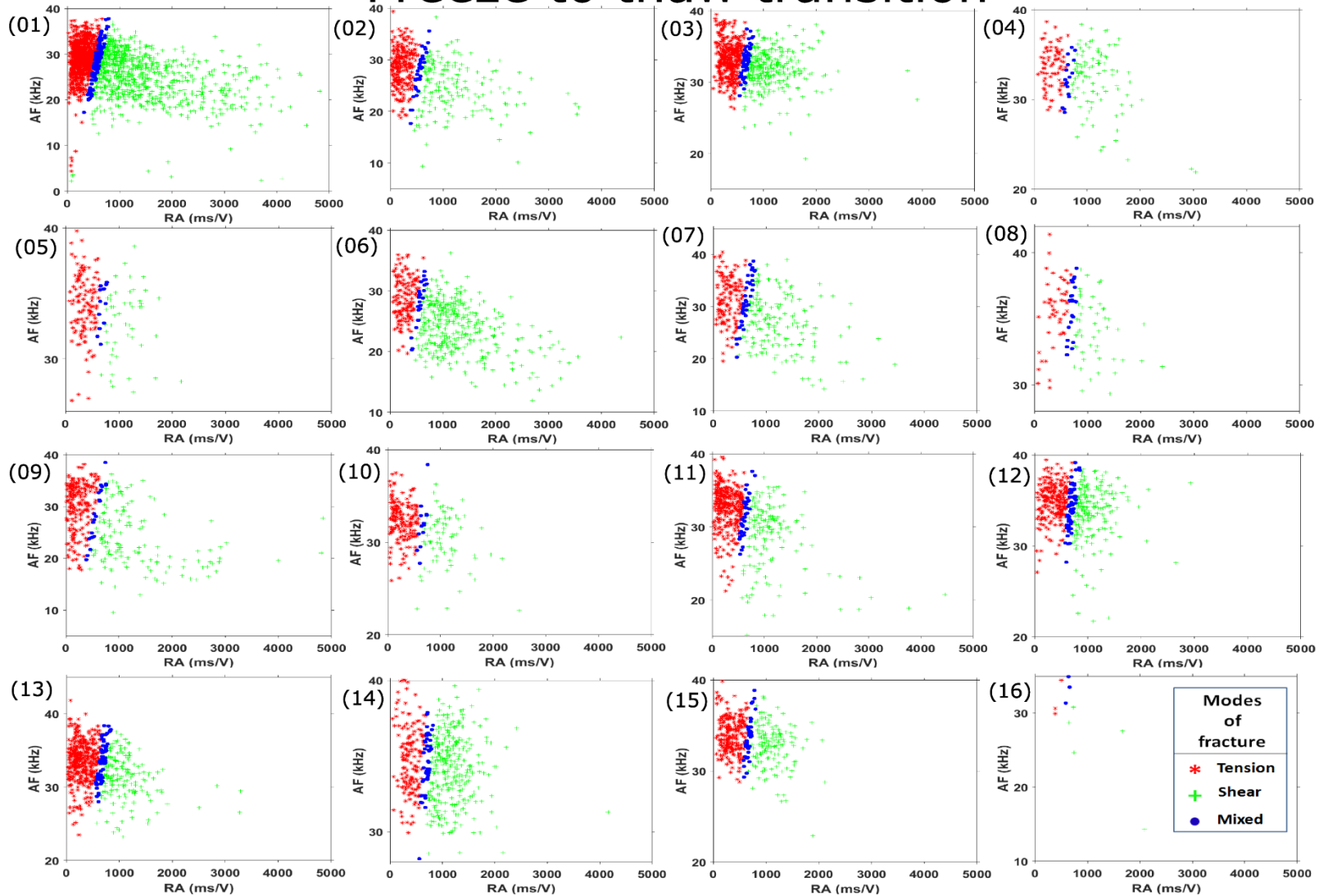


Figure S8. Simplified version of **Figure S7** with AF vs RA values and fracture modes. The number beside each subpanel indicates the number of the respective cycle.

Thaw cycle

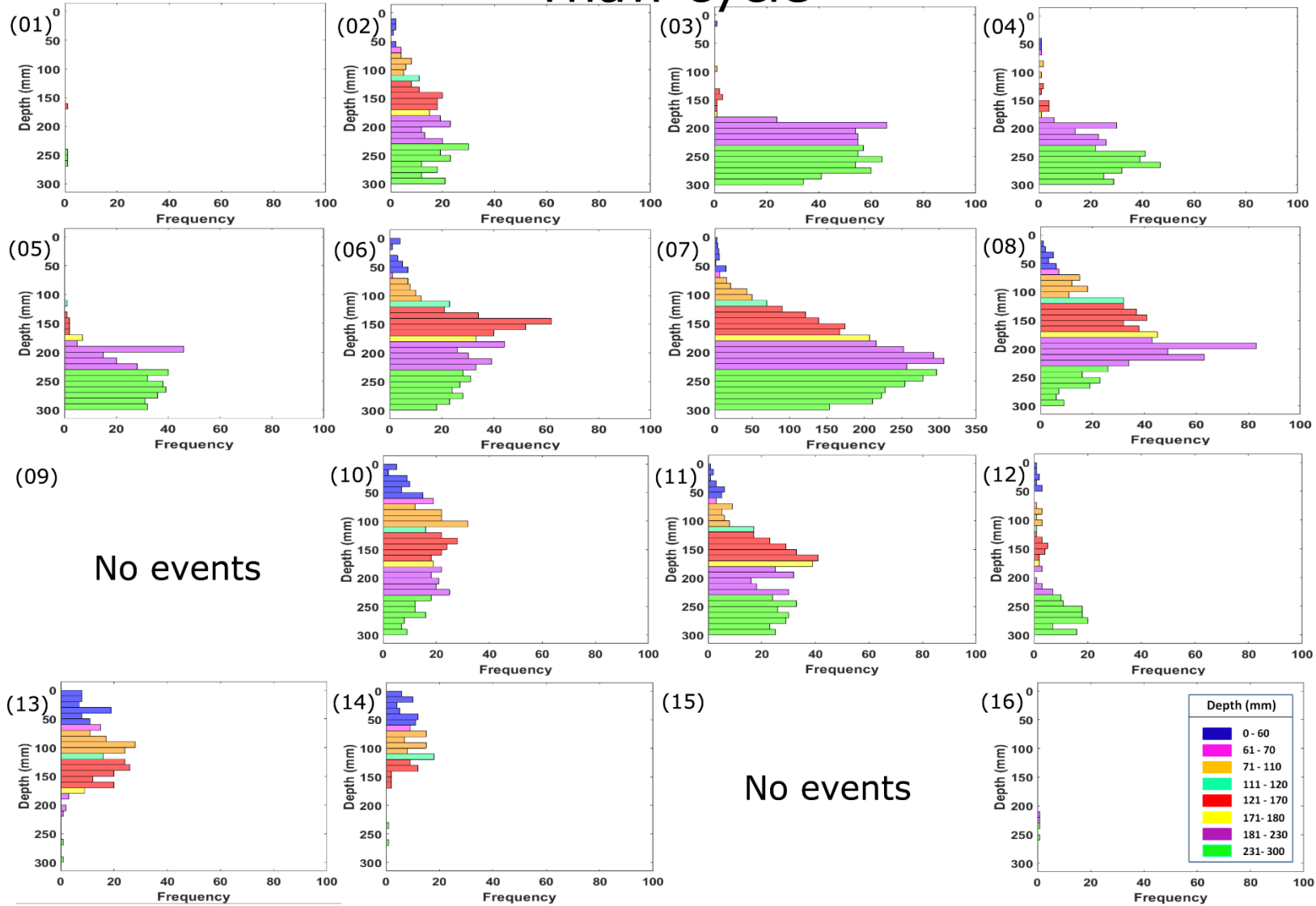


Figure S9. Frequency distribution of AE events along various depth intervals within the block recorded during thawing periods over the course of 16 freeze-thaw cycles. The number beside each subpanel indicates the number of the respective cycle.

Thaw cycle

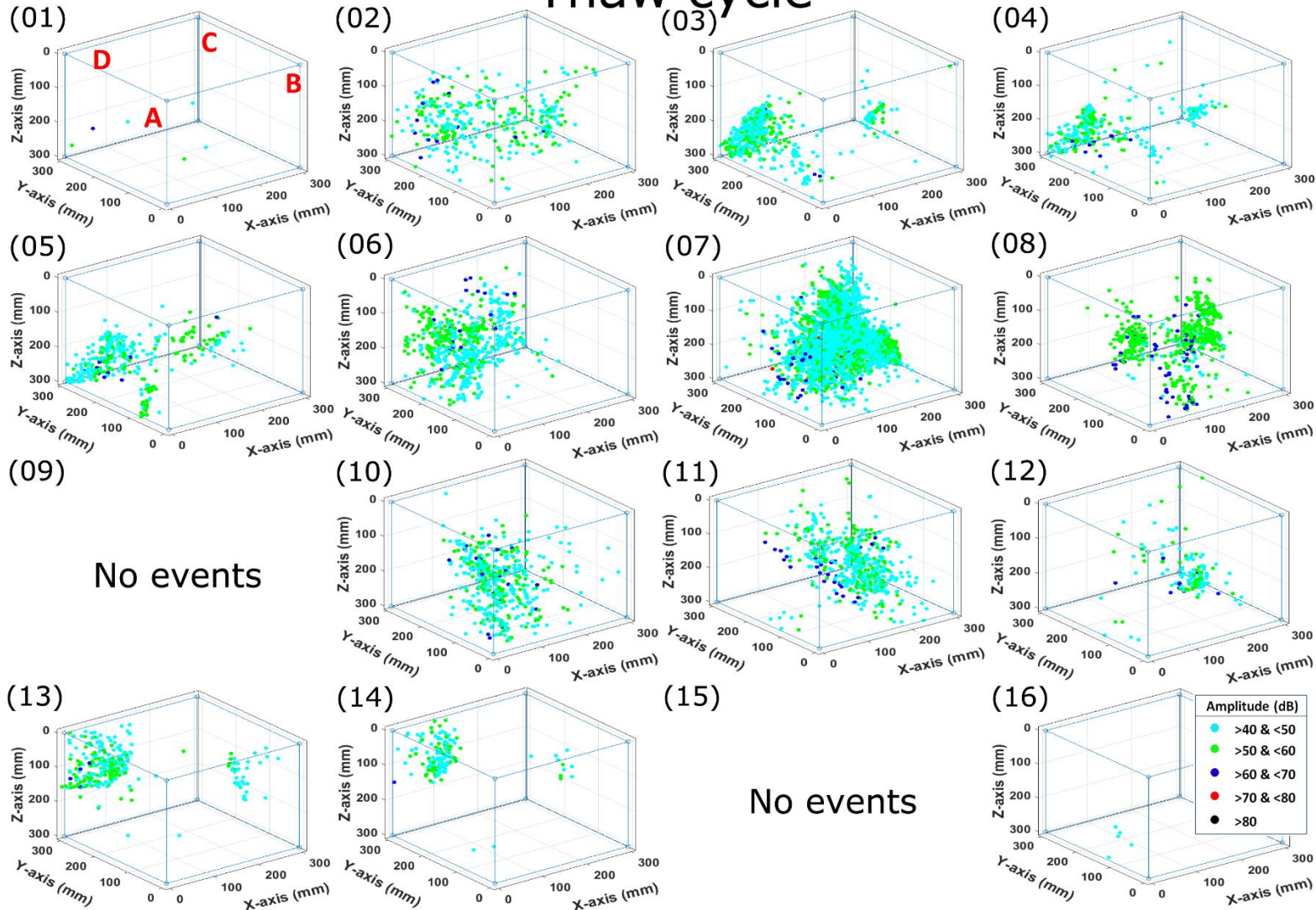


Figure S10. 3D locations of AE events with their respective amplitude recorded during thawing periods over the course of 16 freeze-thaw cycles. Vertical faces A–D of the block are labelled in (01). The number beside each subpanel indicates the number of the respective cycle.

Thaw cycle

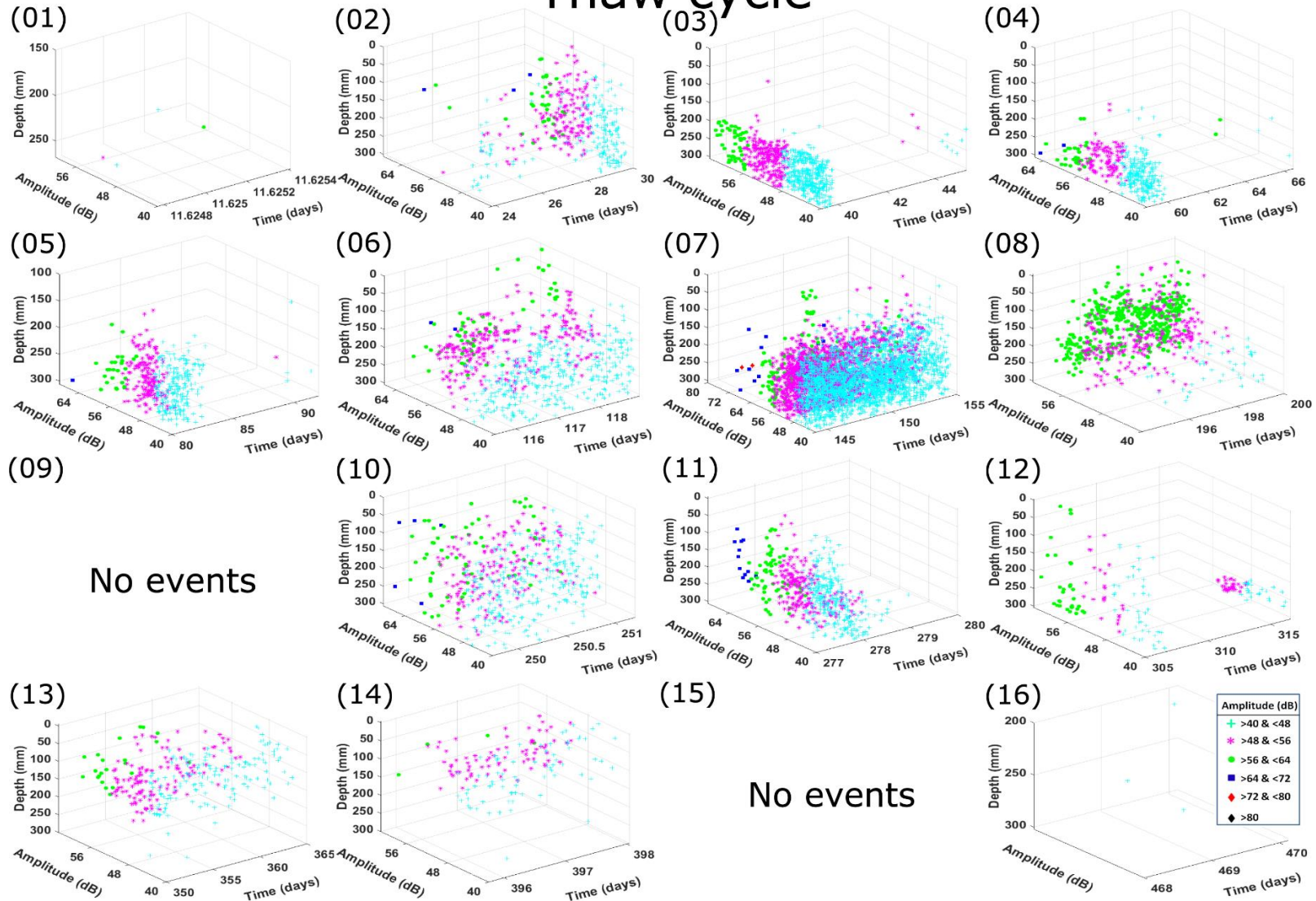


Figure S11. Visualization of AE events in terms of depth, amplitude and time recorded during thawing periods over the course of 16 freeze-thaw cycles. The number beside each subpanel indicates the number of the respective cycle.

Thaw cycle

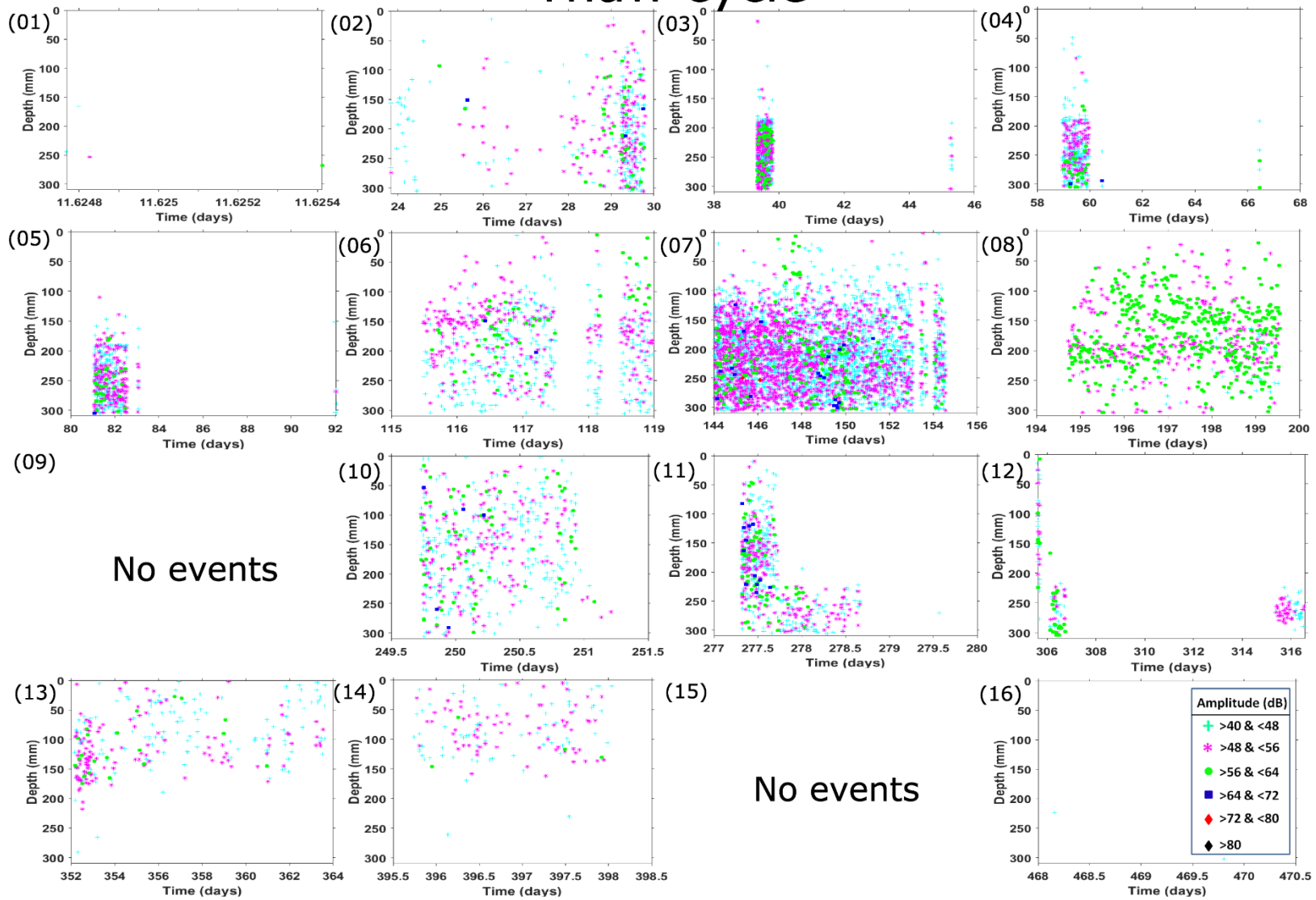


Figure S12. Simplified version of **Figure S11** with depth vs time, and amplitude ranges marked with different shapes and colours. The number beside each subpanel indicates the number of the respective cycle.

Thaw cycle

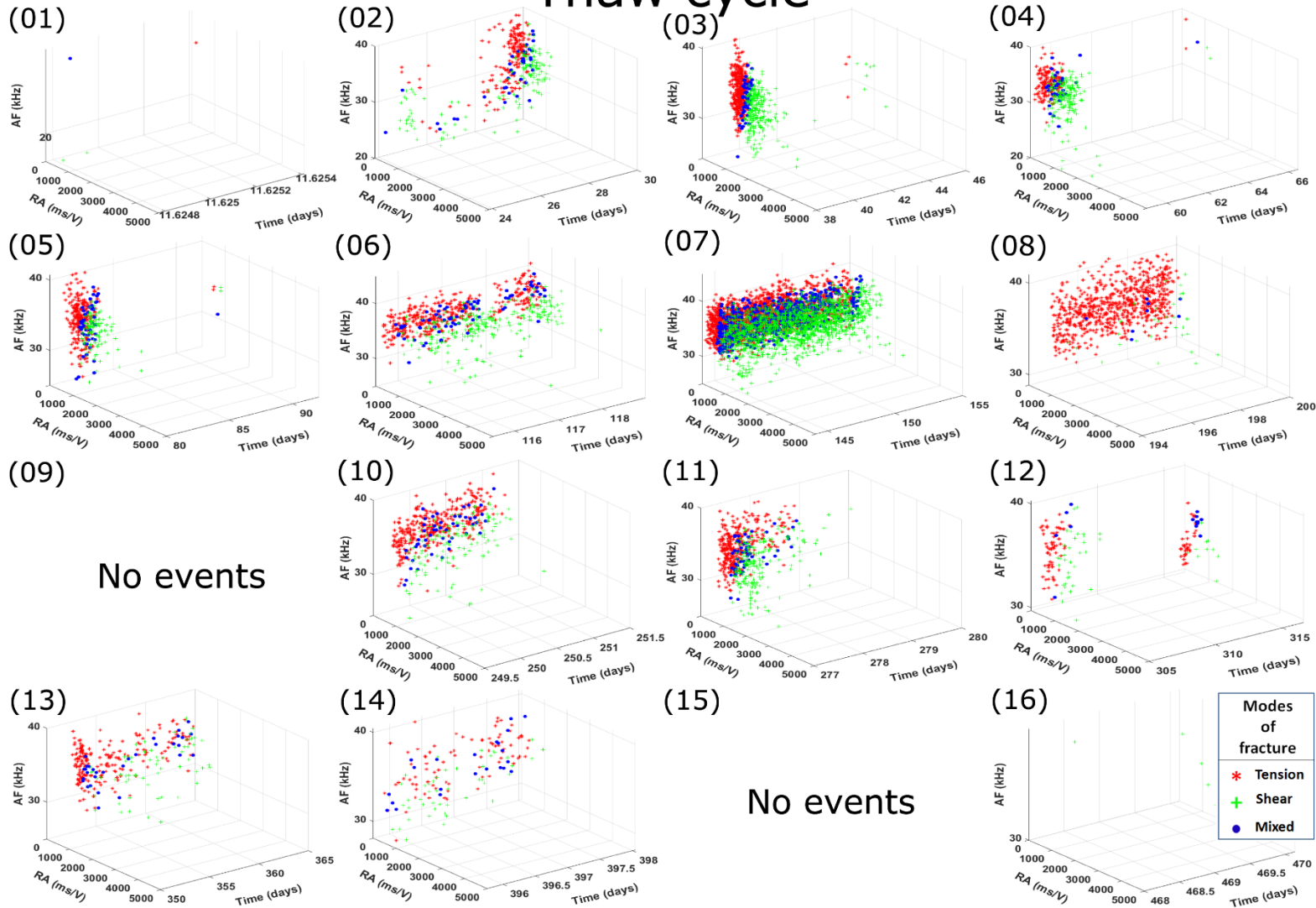


Figure S13. Visualization of AE events in terms of AF values, RA values and time, labelled according to modes of fracture and recorded during thawing periods over the course of 16 freeze-thaw cycles. The number beside each subpanel indicates the number of the respective cycle.

Thaw cycle

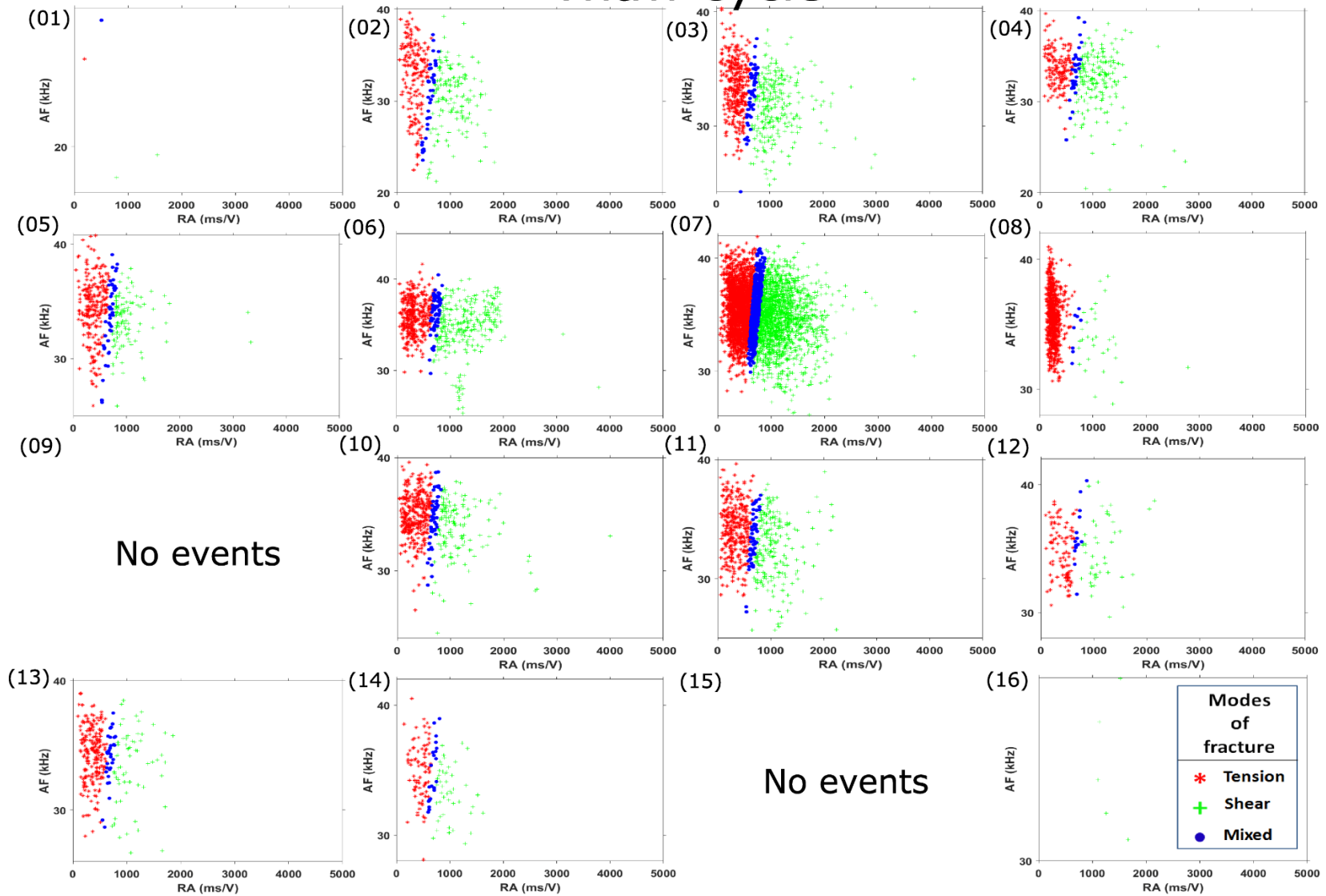


Figure S14. Simplified version of **Figure S13** with AF vs RA values and fracture modes. The number beside each subpanel indicates the number of the respective cycle.

Thaw to freeze transition

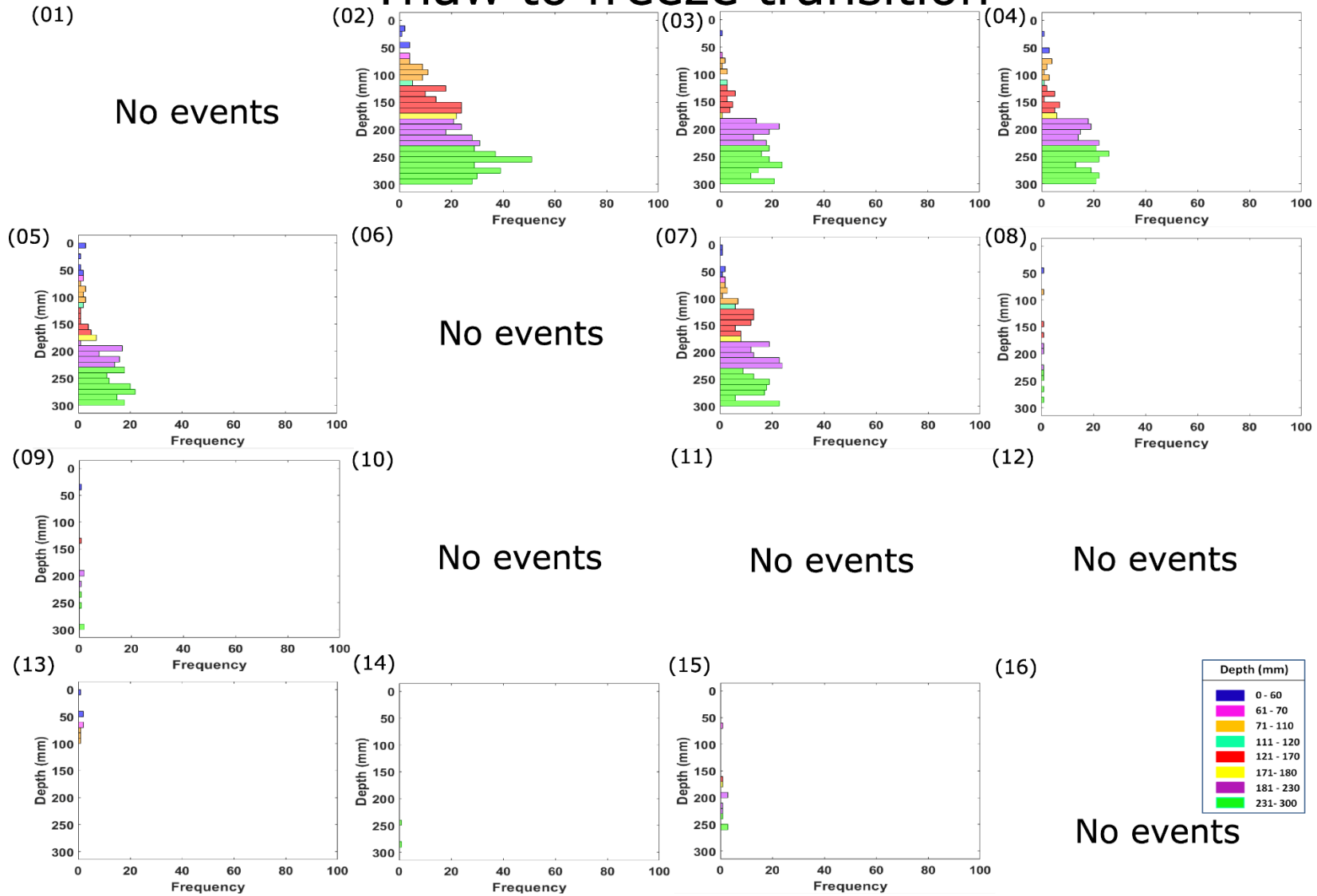


Figure S15. Frequency distribution of AE events along various depth intervals within the block recorded during thaw-to-freeze transitions over the course of 16 freeze-thaw cycles. The number beside each subpanel indicates the number of the respective cycle.

Thaw to freeze transition

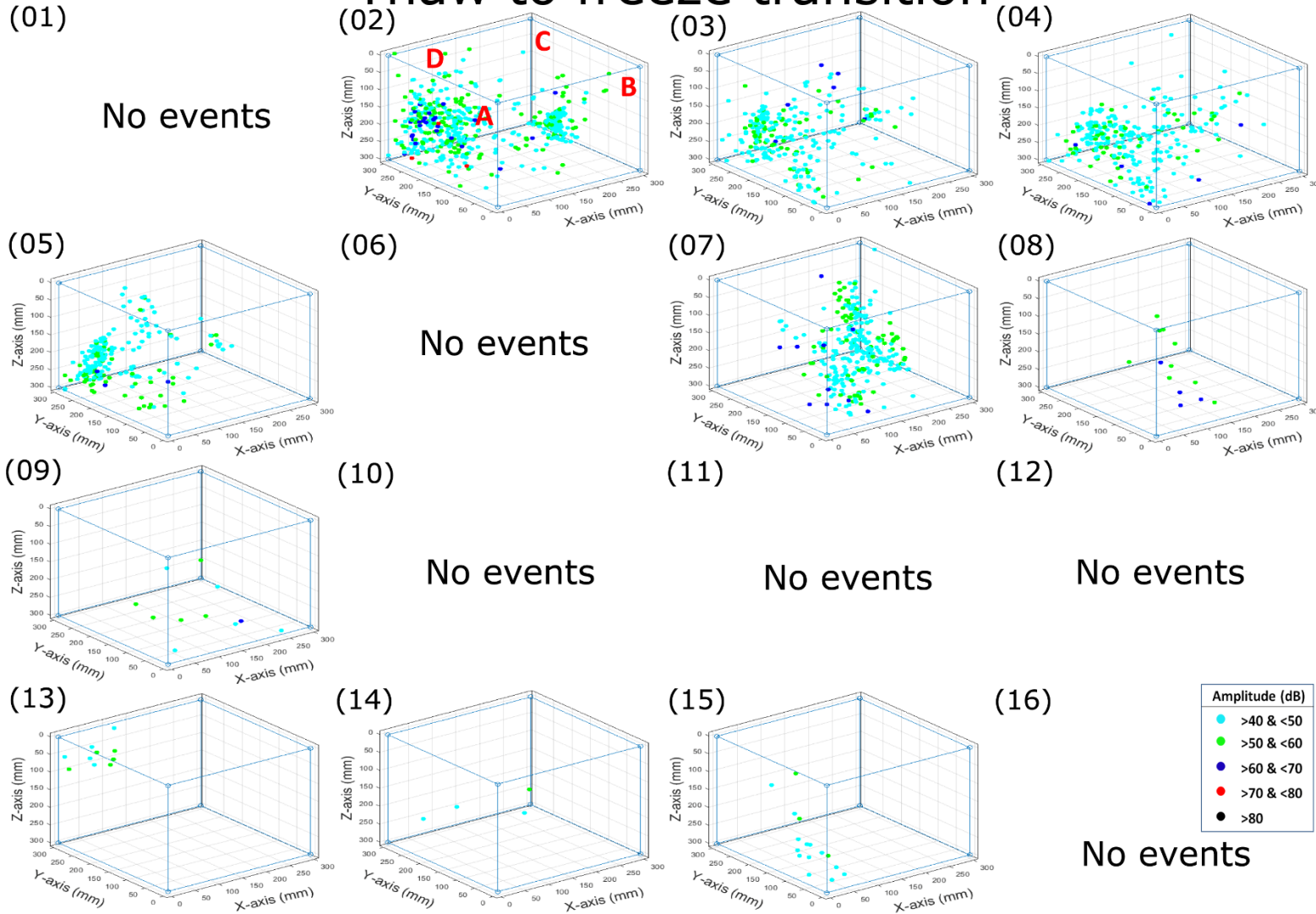


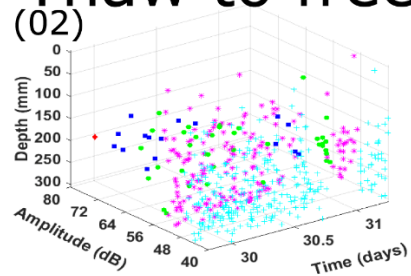
Figure S16. 3D locations of AE events with their respective amplitude recorded during thaw-to-freeze transitions over the course of 16 freeze-thaw cycles. Vertical faces A–D of the block are labelled in (01). The number beside each subpanel indicates the number of the respective cycle.

Thaw to freeze transition

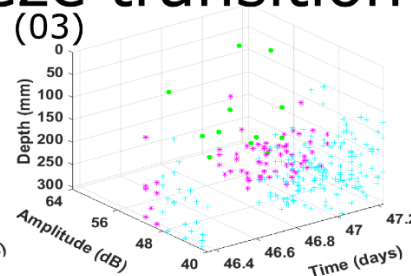
(01)

No events

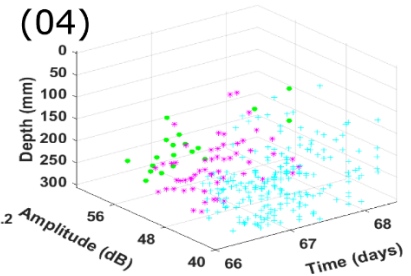
(02)



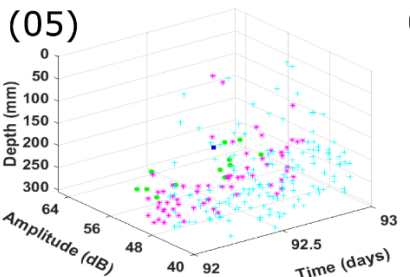
(03)



(04)



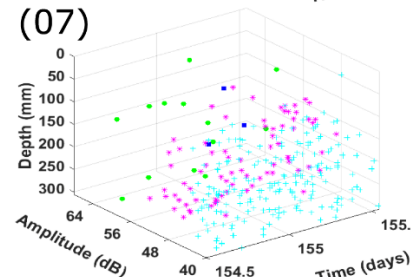
(05)



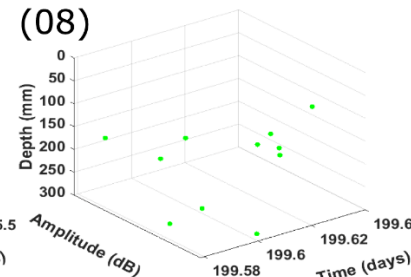
(06)

No events

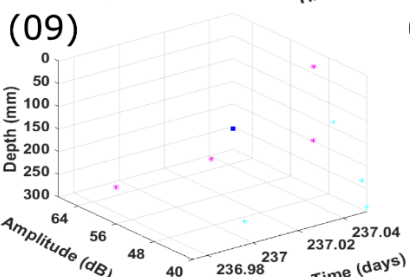
(07)



(08)



(09)



(10)

No events

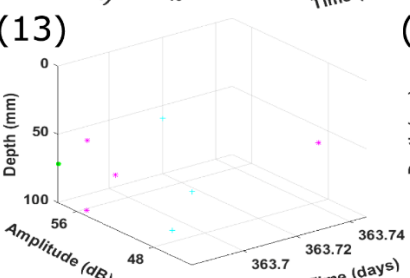
(11)

No events

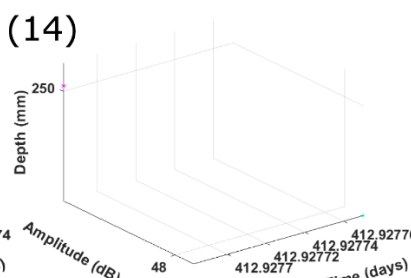
(12)

No events

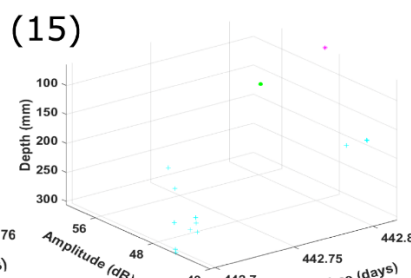
(13)



(14)



(15)



(16)

No events



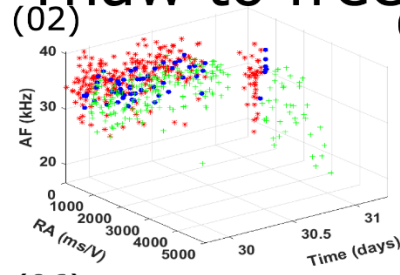
Figure S17. Visualization of AE events in terms of depth, amplitude and time recorded during thaw-to-freeze transitions over the course of 16 freeze-thaw cycles. The number beside each subpanel indicates the number of the respective cycle.

Thaw to freeze transition

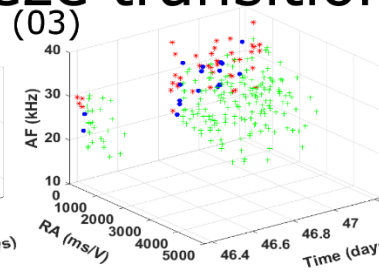
(01)

No events

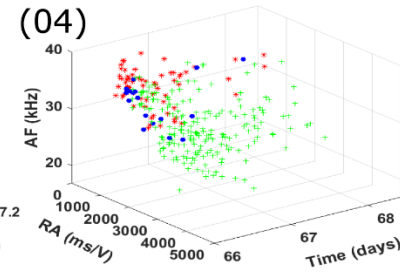
(02)



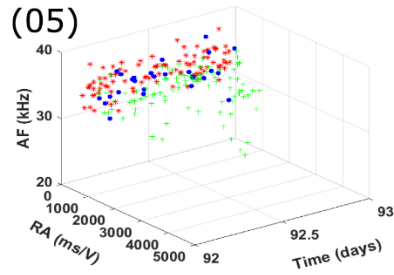
(03)



(04)



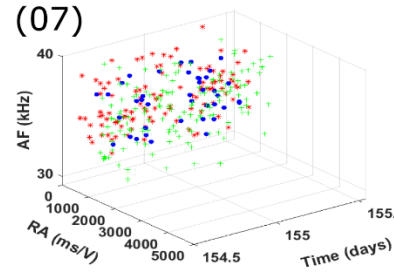
(05)



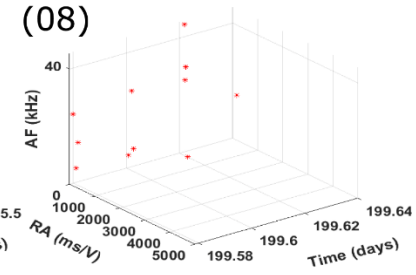
(06)

No events

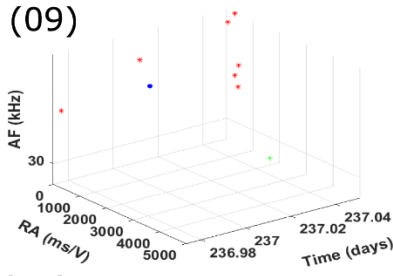
(07)



(08)



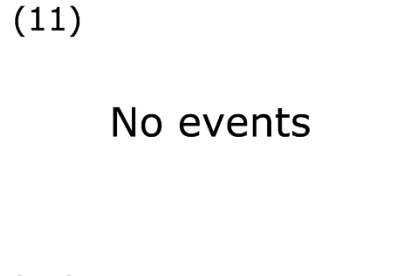
(09)



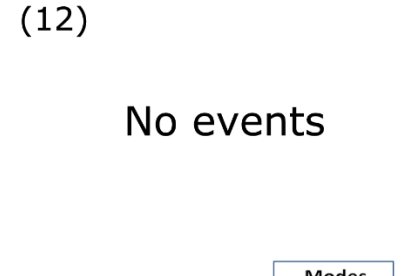
(10)

No events

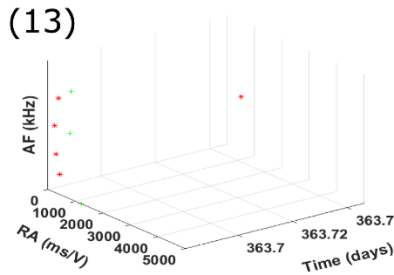
(11)



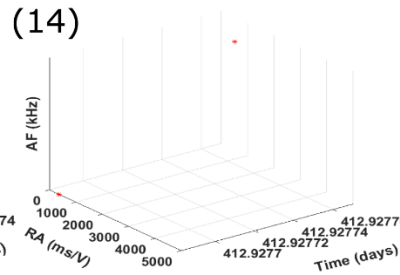
(12)



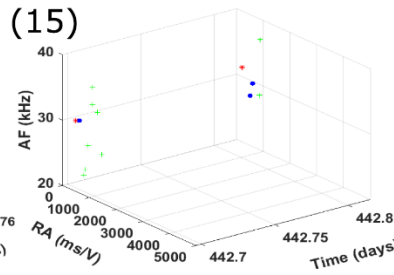
(13)



(14)



(15)



(16)

No events



Figure S18. Visualization of AE events in terms of AF values, RA values and time, labelled according to modes of fracture and recorded during thaw-to-freeze transitions over the course of 16 freeze-thaw cycles. The number beside each subpanel indicates the number of the respective cycle.

Thaw to freeze transition

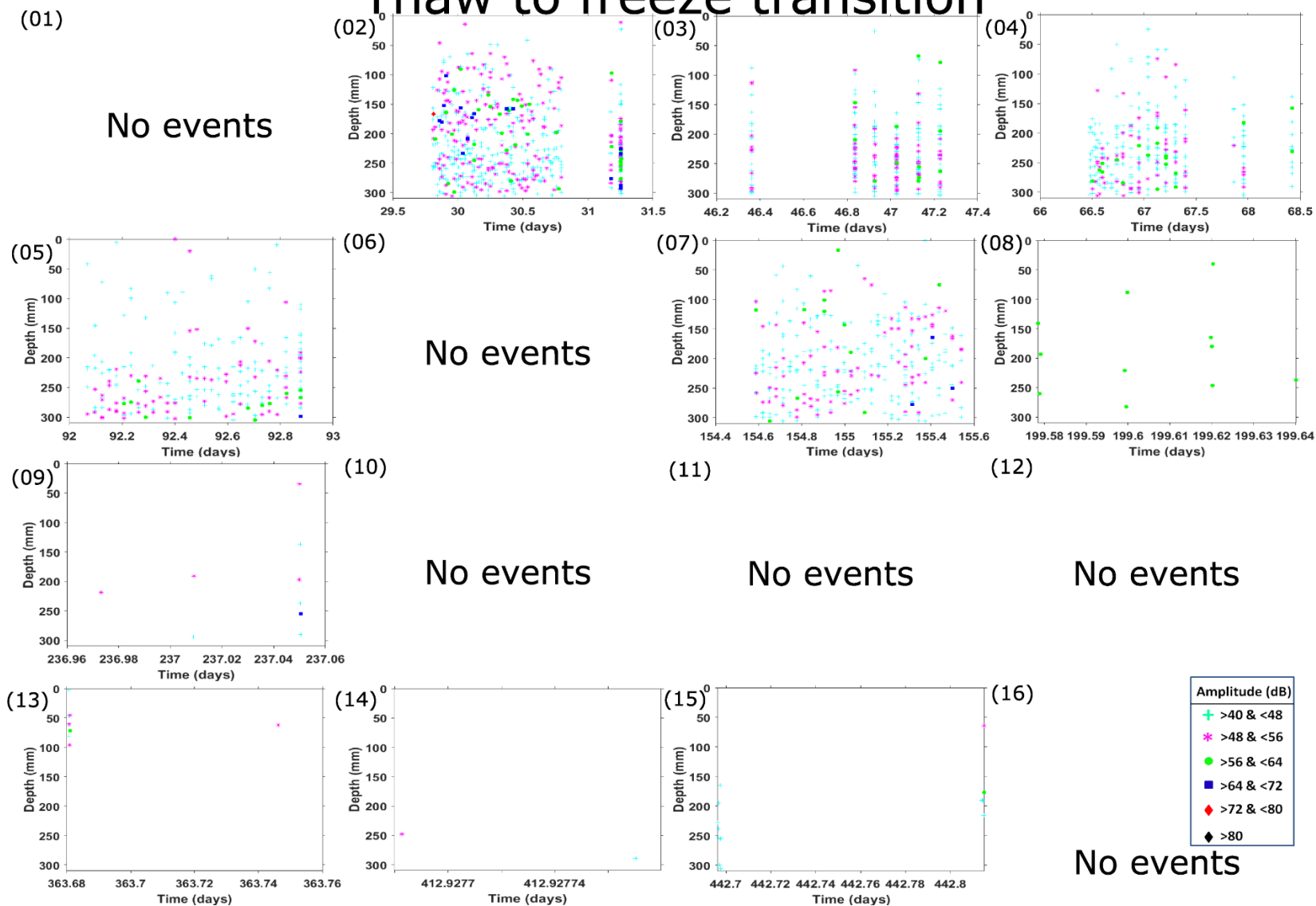


Figure S19. Simplified version of Appendix 17 with depth vs time, and amplitude ranges marked with different shapes and colours. The number beside each subpanel indicates the number of the respective cycle.

Thaw to freeze transition

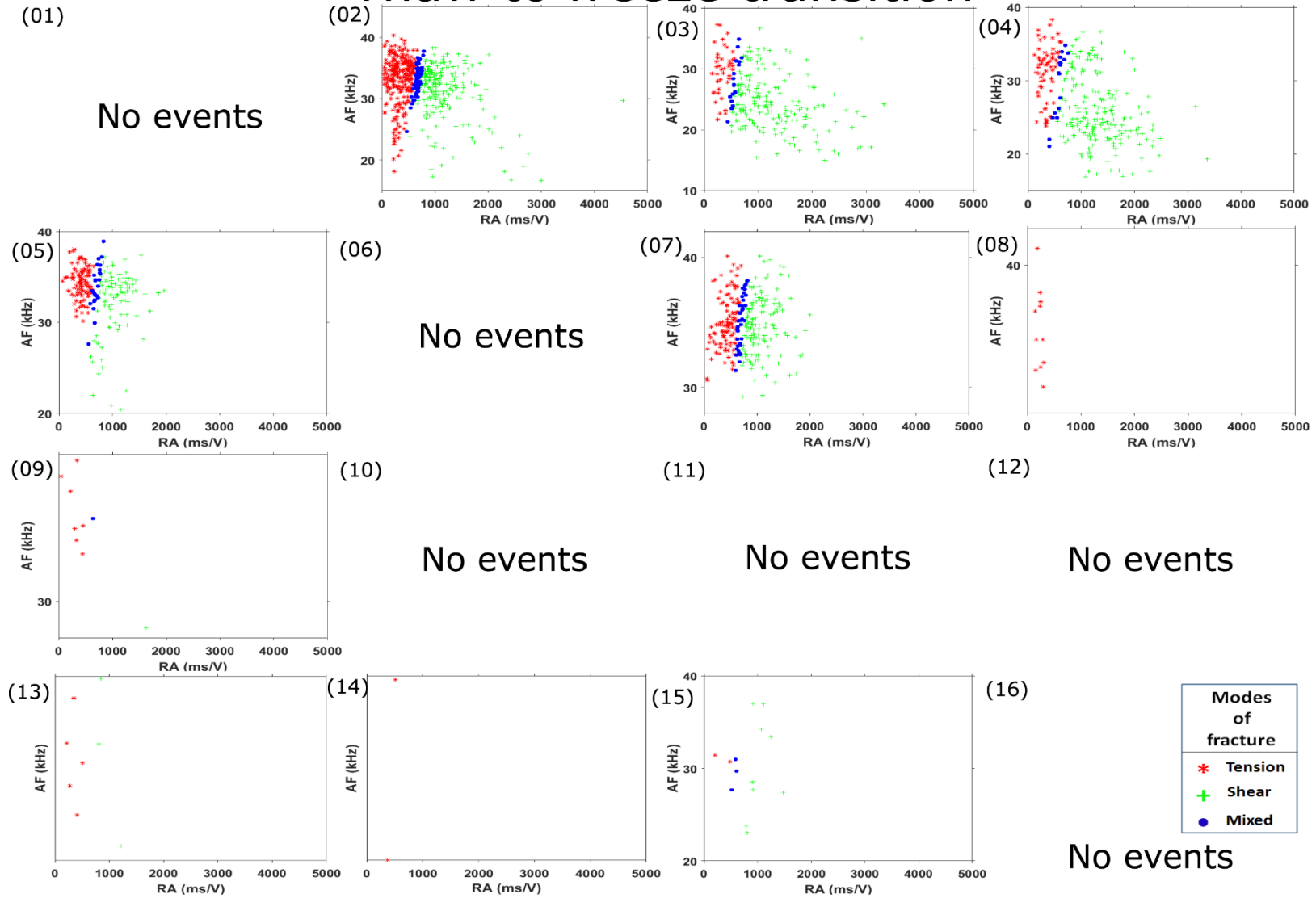


Figure S20. Simplified version of **Figure S18** with AF vs RA values and fracture modes. The number beside each subpanel indicates the number of the respective cycle.